34

Remote Sensing Rock Mechanics and Earthquake Thermal Infrared Anomalies

Lixin Wu[1,2] and Shanjun Liu[2]
[1]*Academy of Disaster Reduction & Emergency Management, Beijing Normal University, Beijing, China*
[2]*Institute for Geo-informatics & Digital Mine Research, Northeastern University, Shenyang, China*

1. Introduction

Rock fracturing is the cause of many geo-hazards including tectonic earthquake (EQ), rock burst, rock sloping and rock pillar failure. Radiation signals such as acoustic emission, radio frequency emission and electromagnetic (EM) radiation from loaded deforming rock, are able to provide useful information for monitoring, interpreting and predicting rock fracturing (Renata, 1977; Brady and Rowell, 1986; Yamada et al., 1989; Martelli et al., 1989). Based on thermo-elastic theory, thermo-elastic stress analysis (TSA) and stress pattern analysis by thermal emission (SPATE) were developed for the stress measurement of solid materials, including homogeneous metal, macromolecular and composite materials, respectively in 1960's and 1970's (Mounatin and Webber, 1978). Luong applied thermovision to study experimentally the damage processes of concrete and rock (Luong, 1990), but no reach to the remote sensing on geo-hazards.

In the experiments for investigating the mechanism of satellite thermal infrared (TIR) anomaly before tectonic EQ (Gorny et al., 1988; Qiang et al., 1990), it was discovered that there do exist TIR anomaly before rock fracturing (Geng et al., 1992). Later, it was furthermore discovered that there are obvious TIR features as precursors of rock fracturing, and that the loaded stress around $0.79\sigma_c$ can be taken as a precaution index for the stability monitoring of loaded rocks (Wu and Wang, 1998). To explore the laws of infrared radiation (IRR) variation in the process of rock loading, deforming and fracturing, and to reveal the possible mechanism of satellite TIR anomaly before EQ, a large amount of IRR imaging experiments on rock loaded to fracturing were conducted in China (Wu et al., 2000, 2001, 2002, 2003, 2004a, 2004b, 2004c, 2004d, 2006a, 2006b; Deng et al., 2001; Liu et al., 2002). Hence, a new intersection discipline, Remote Sensing Rock Mechanics (RSRM), which takes Remote Sensing, Rock Mechanics, Rock Physics and Informatics as its foundations and serves for remote sensing on geo-hazards, was originated (Geng et al., 1992; Wu et al., 2000).

Based on retrospection to past experiments on RSRM, it was pointed out that there are two IRR anomalies, being IRR image anomaly and IRR temperature curve anomaly respectively, can act as rock fracturing precursors. The average IRR temperature (AIR*T*), being the

integral reflection of surface IRR energy, is applied as a quantitative index to study the temporal evolution of IRR from loaded rock and to seek for the potential precursors of rock fracturing. The temporal evolution of AIR*T* are the comprehensive effect of a series of physical-mechanical processes inside a loaded rock, such as rock thermo-elastic acting, pore gas desorbing & escaping, fractures producing & extending, rock frictionating, heat transferring and environment radiation. The thermo-elastic effect and the frictional thermal are two of the main mechanisms of increased IRR from loaded rock. RSRM experiments had revealed the laws of changed IRR from loaded rock and provided scientific interpretations for the mechanisms of satellite TIR anomaly before tectonic EQs of Ms>5.5.

2. Remote Sensing Rock Mechanics Experiments

2.1 Experiment Methods and Tools

The typical RSRM experiment is comprised of a loader (uni-axial or bi-axial), an infrared imager and rock samples. As in Figure 1, a bi-axial loader was applied for loading along two directions, and an infrared imager was applied to detect the surface IRR from loaded rock. The maximum imaging rate of the imager is 60f/s, and the recording rate was usually set as 1f/s to record the IRR images continuously. Usually, tectonic EQ might be resulted from the suddenly fracturing of compressively-sheared crust rock, the suddenly breaking of faults at disjointed zones, the suddenly sliding of compressively-sheared faults or the stability losing of compressively loaded intersected faults. To simulate the different mechanisms of rock fracturing and EQ, several typical loading schemes were applied as in Figure 1.

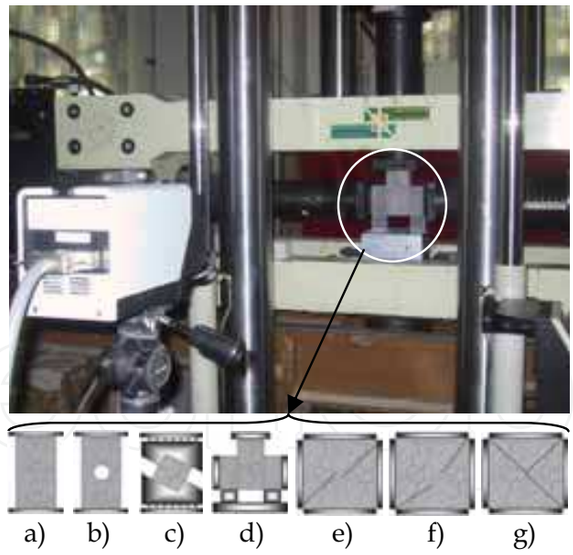

Fig. 1. RSRM experiment schemes to simulate different mechanisms of rock fracturing or tectonic EQ: a) uni-axially load on a standard cylinder rock sample; b) uni-axially load on a cylinder rock sample with a central hole; c) compressively-sheared load on a hexahedral rock sample; d) bi-axially load on three jointed rock samples to frictional sliding; e) bi-axially load on a damage rock sample with en echelon faults; f) bi-axially load on a damage rock sample with disjointed faults; and g) bi-axially load on three jointed rock samples simulating intersected faults.

2.2 Rock Fracturing Precursor: IRR Image Anomaly

2.2.1 Uni-axially loaded rock

Lots of rock samples made from coal, ironstone, sandstone, marble, limestone, granite, granodiorite, gabbro and gneiss were uni-axially loaded and thermal imaging detected. The sample size was standard of diameter and length, respectively, 50 and 100mm. It was discovered that the IRR images of the uni-axially loaded rock have different features for different fracturing pattern (Wu et al., 2006a). As in Figures 2~4, there are three fracturing patterns, "X"-shaped, "//"-shaped and "|"-shaped respectively, occurred in our experiments. The "X"-shaped and "//"-shaped positive IRR abnormal strips foretell the coming of "X"-shaped shearing fracturing and the coming of "//"-shaped shearing fracturing respectively, while the "|"-shaped negative IRR abnormal strip foretells the coming of tensile fracturing.

The "X"-shaped positive IRR abnormal strips generated with loading along the "X"-shaped shearing zone before peak stress, and got distinguished after peak stress, as in Figure 2. The rock sample got finally fractured along the "X"-shape shearing zone. The evolution of IRR abnormal strip had also reflected the fracturing being not symmetrical upper-and lower, in that the upper part was clear with higher temperature, while the lower part is fuzzy with lower temperature.

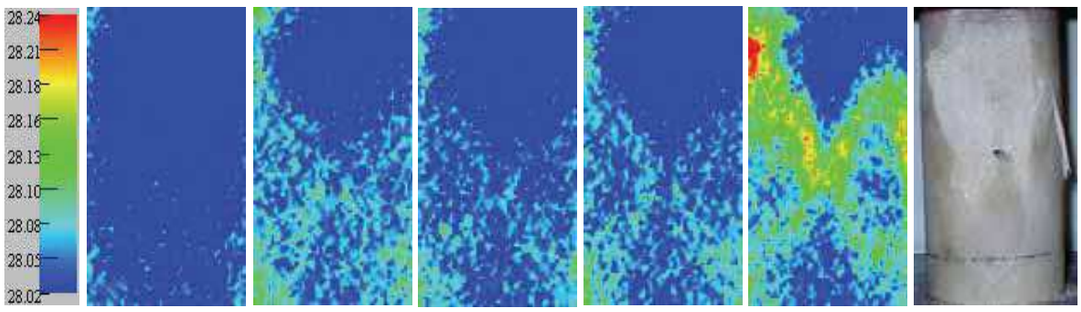

Fig. 2. The IRR image positive anomaly of "X"-shaped shearing fracturing of an uni-axially loaded marble sample

The "//"-shaped positive IRR abnormal strips generated with loading along the "//'-shaped shearing zone at the upper part of sample before peak stress, and got distinguished after peak stress, as in Fig 3. The evolution of the positive IRR image anomaly had also reflected the fracturing being not symmetrical in that the upper part of the IRR anomaly strip was clear with higher temperature, while the lower part was fuzzy excepting for the final fracturing near the bottom of the sample. Besides, there was strong IRR anomaly spot at the fracturing center for the intensive accumulation of mechanical energy and for the intensive generation of frictional thermal at the local central place.

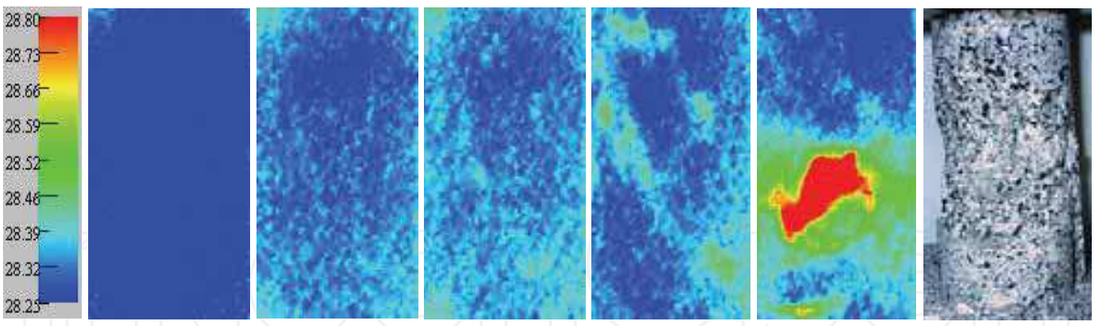

Fig. 3. The IRR image positive anomaly of "//"-shaped shearing-fracturing of an uni-axially loaded granite sample

The "|"-shaped negative IRR abnormal strip generated with loading along the tensile fracturing zone of a rock sample before the peak stress, and got distinguished gradually at the peak stress and after fracturing, as the approximately vertical dark strip in Figure 4. The same phenomenon for a sandstone sample with a calcite vein was also reported (Wu, et al., 2000).

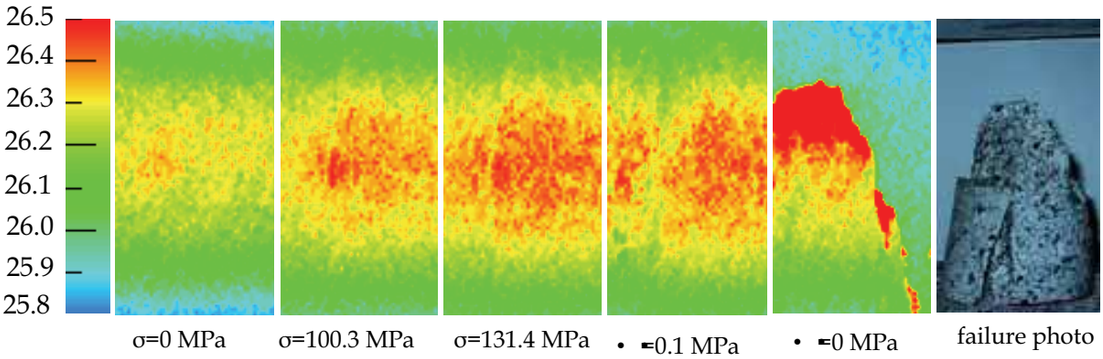

Fig. 4. The IRR image negative anomaly of "|"-shaped tensile fracturing of an uni-axially loaded granite sample

2.2.2 Uni-axially loaded rock with a central hole

More than 10 samples with a central hole, modeling the structure stability of loaded rock tunnels, made from marble and granite were infrared imaging detected. The rock samples had two kinds of shapes respectively being cylinder with diameter and length, respectively, 50 and 100mm, and regular block with thickness, width and length, respectively, 70, 35 and 100 mm. It was discovered that there were distinguished positive IRR image anomalies before rock fracturing, and the place of anomaly were exactly the coming fracturing place. As in Figure 5, the positive IRR image anomalies had reflected the two kinds of fracturing, respectively being diagonal fracturing (sample 1~5) and fork fracturing (sample 6). The IRR anomalies, along the fracturing planes and shaped as spots or strips, generated not only on rock surface but also on the hole's surface (lateral sample 4 and 5). The temperature increment is 1~3^{o}C and 4~8^{o}C respectively for marble and granite samples.

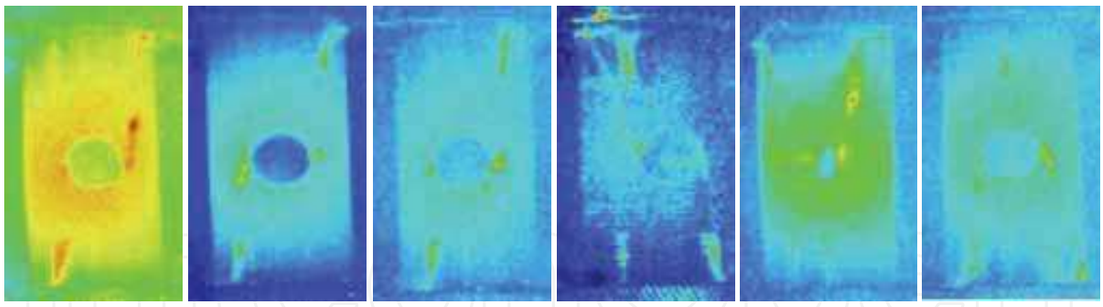

Fig. 5. The IRR image positive anomalies of a group of uni-axially loaded marble samples with a central hole

2.2.3 Compressively sheared rock

More than 20 samples, size 7×7×7×cm^3, made from sandstone, marble, limestone, granite and gneiss, were compressively sheared and infrared imaging detected. Three pairs of steel platens with shearing angle being 45°, 60° and 70° respectively were applied. The loading rate was controlled as 2~5kN/s. It was discovered that the IRR temperature of rock surface changed with loading, and a strip-shaped positive IRR image anomaly generated along the central shearing plane before fracturing. With loading, the positive abnormal strip got more and more distinguished and migrated gradually from the upper end to the lower end of the sample, which foretold that the compressive-shearing fracturing was developing gradually from the upper end to the lower end of the sample along the central shear plane. Figure 6 shows the typical IRR image series of a compressively sheared limestone sample.

As a special geological phenomenon occurring with the formation of great fault, penniform-shaped fractures are a group of secondary fractures produced with the formation of great primary fracture (Nicolas et al., 1977). It happened to occur in our experiments that there were penniform-shaped fractures produced with a primary fracture in the compressive loaded rock samples, as in Figure 7. The IRR positive anomaly strips generated aside the primary IRR strip, passing through the central shearing plane, had reflected the penniform-shaped fracturing events.

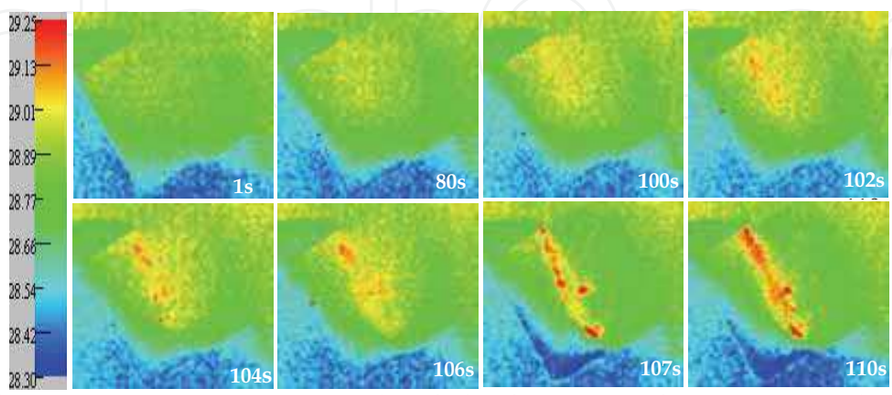

Fig. 6. The IRR image positive anomaly of the fracturing of a compressively sheared limestone sample (time in second)

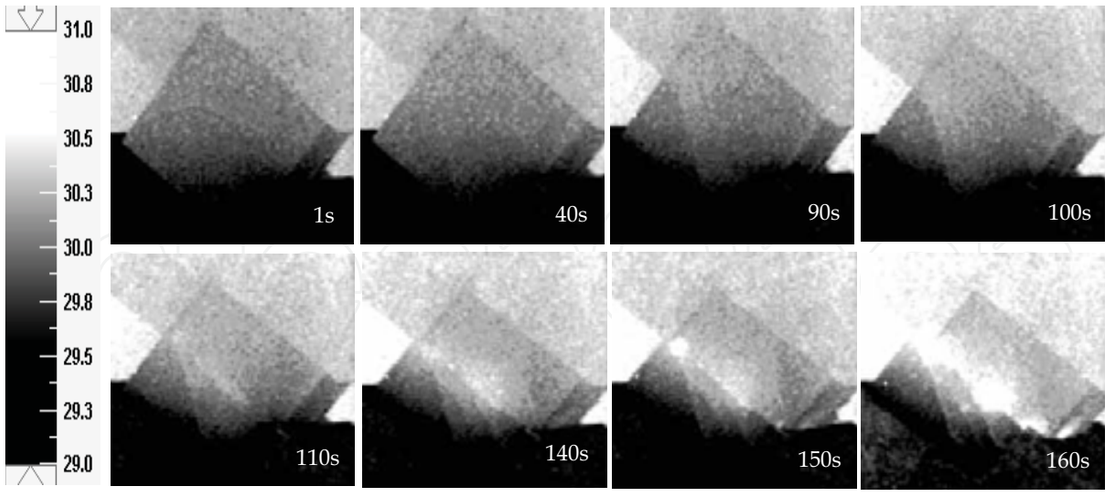

Fig. 7. The IRR image anomaly of the penniform-shaped fracturing of a compressively sheared marble sample

2.2.4 Bi-sheared frictional sliding rock blocks

Ten groups of rock samples made from gabbro, granodiorite, limestone and marble were IRR detected in the process of bi-sheared frictional sliding or viscosity sliding. Each group, as in Figure 8 and 9, was comprised of three jointed rock blocks whose size respectively be 50• 50• 100mm^3, 50• 70• 150mm^3 and 50• 50• 100mm^3 from left to right, and its friction area was constant, 50• 100mm^2. Four contact conditions, symmetrical (yes for rock property and for its smooth friction surface, as in Figure 8), uncertain symmetrical (yes for rock property but not for its coarse friction surface, as in Figure 9), unstable asymmetrical (yes for rock property but not for its staged friction surface) and stable asymmetrical (not for rock property but yes for its smooth friction surface), were designed and tested respectively (Wu et al., 2004b).

It is revealed that the evolution of rock surface IRR temperature field is not only correlated with rock stress, but also correlated with the features of friction surface and rock properties at both sides. General law lies in that the IRR at the place of stress concentration and strong friction zone is stronger than that at the place of stress relaxation and weak friction zone. In condition of friction surface be symmetrical, the IRR image is double butterfly-wings shaped, as in Figure 8. However, in condition of friction surface be uncertain symmetrical, unstable asymmetrical or stable asymmetrical, the temporal-spatial evolution of IRR anomaly is uncertain or unstable, as in Figure 9. The positive IRR anomaly spots, foretelling the evolution of stress, energy and viscosity-sliding process, may be beads-shaped, needle-shaped, suspended needle-shaped, strip-shaped, single butterfly-wings shaped or its evolution in order (Wu et al., 2004b).

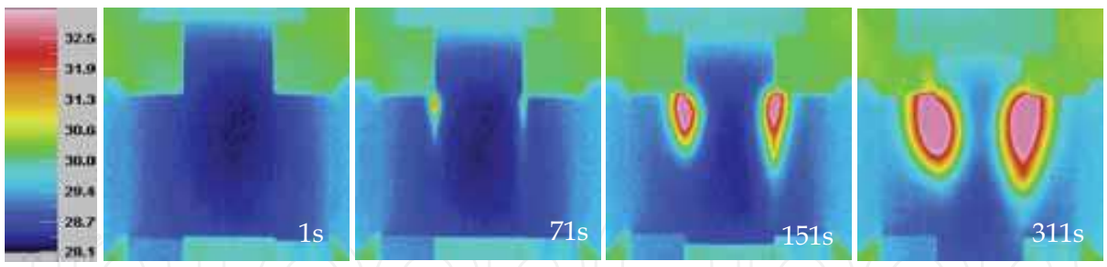

Fig. 8. The IRR image positive anomaly of the stick-slipping of symmetrical rock samples (time in second)

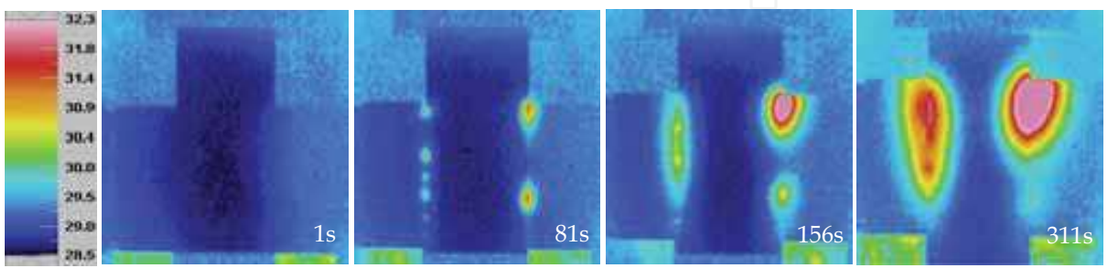

Fig. 9. The IRR image positive anomaly of the stick-slipping of asymmetrical rock samples (time in second)

2.2.5 Bi-axially loaded rock

Infrared imaging detection on the rupturing of en echelon and collinearly disjointed jointed faults were done in the process of bi-axial loading. It was revealed that the IRR from loaded rock surface is correlated with loading stress, which could be divided into five stages as loading beginning, linear elastic, stress locking, stress unlocking and fracturing(Wu et al., 2004a). During the stress-unlocking stage, positive IRR anomaly strip generated at the disjointed zone, as in Figure 10 and 11. The positive IRR anomaly strip around the disjointed zone has general evolution features as: firstly, the strip gets enhancing; then, gets weakening (or 'silence'); and finally, gets enhancing again. The re-enhancing of IRR anomaly strip after the weakening stage is a meaningful precursor foretelling the place of primary fracturing of faults or the coming epicenter of an EQ.

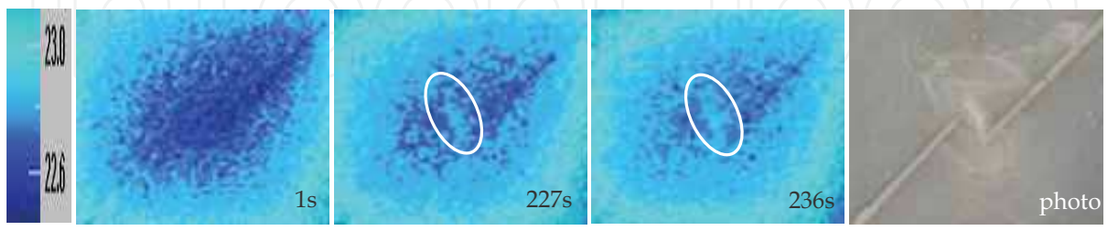

Fig. 10. The local IRR positive anomaly foretell the fracturing of en echelon disjointed faults (marble, time in second)

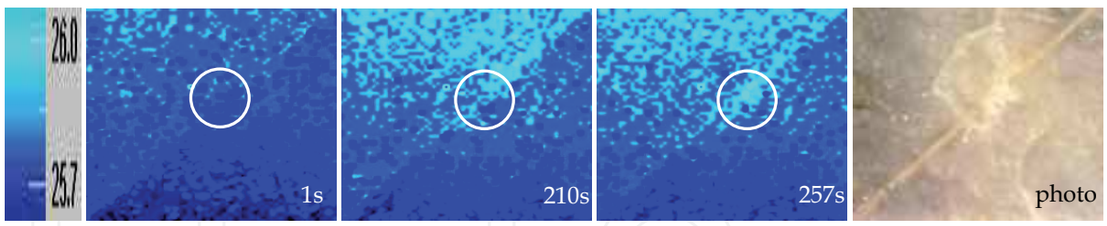

Fig. 11. The local IRR positive anomaly foretell the fracturing of collinearly disjointed faults (marble, time in second)

2.3 Rock Fracturing Precursor: IRR Temperature Anomaly

2.3.1 Quantitative index: AIR*T*

The evolution of surface IRR from loaded rock is the comprehensive effect of rock thermo-elastic acting, pore gas desorbing & escaping, fractures producing & extending, rock frictionating, heat transferring and environment radiation. Being the integral reflection of surface IRR energy, the average IRR temperature (AIR*T*) is selected as a quantitative index to study the evolution of IRR from loaded rock and to seek for rock fracturing precursors (Wu et al., 2006b).

The infrared imager detects and records the thermal images of loaded rock surface. The thermogram is comprised of a matrix of color pixels which representing the IRR brightness temperature of each pixel of the rock surface. For example, the imaging matrix of TVS-8100MKII infrared imager is 160• 120. The IRR temperature of each pixel tends to fluctuate with time due to the instability of the detector unit and the influence of environmental radiation, and the IRR temperature of each pixel will not always be the same for the local difference of rock stress and rock strain. The maximum, minimum and average value of loaded rock surface IRR temperature, respectively being IRRT_{max}, IRRT_{min} and IRRT_{ave}, could be quantitatively obtained from thermogram. The analysis revealed that IRRT_{max} and IRRT_{min} will not change obviously except that IRRT_{max} might rise suddenly just before rock fracturing, while IRRT_{ave} is to change stably with loading, as in Figure 12. The physical interpretation lies in that the surface IRRT_{ave} is a general reflection of the energy balance inside the loaded rock.

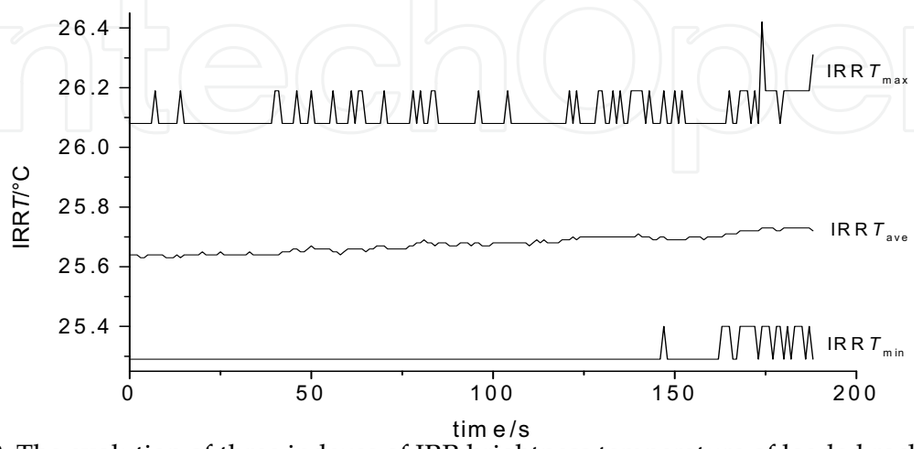

Fig. 12. The evolution of three indexes of IRR brightness temperature of loaded rock surface

Hence, the IRRT_{ave} of rock surface, denominated as AIR*T*, is selected as a quantitative index to study the precursors of rock fracturing and geo-hazards. The procedures for AIR*T*-based precursor analysis includes: 1) to define a unified boundary of the analyzed region (resampling region) for all thermogrames; 2) to resample the IRR temperature value from the data file of each thermograme in time order; 3) to calculate the AIR*T* of the resampling region of each thermograme; 4) to draw the AIR*T*–time curve of the rock sample; 5) to analyze the evaluation features of the AIR*T*–time curve and to identify the messages as a precursor of rock fracturing and hazard; 6) to compare with the qualitative image anomaly so as to analyze and to confirm the AIR*T* abnormal precursor.

2.3.2 Influence factors of AIR*T* curves

1) Loading stages and rock deformation

The stress-strain curve is a basic method for describing rock deformation and for interpreting rock mechanical behaviors (Hudson and Harrison, 1997). Generally, the deformation process of loaded rock is divided into four stages respectively being stage-I of defects compaction, stage-II of linear elastic deformation, stage-III of plastic deformation and stage-IV of fracturing failure, as in Figure 13. The four characteristic points, E, Y, P and F are called as elastic-starting point, yield-starting point, peak-stress point and failure-impending point respectively.

Stage-I: the downward-concave curve section tells that there are some defects such as pores, fissures and joints inside the rock body, and that the defects is under compaction, which cause the stress to rise slowly. The more the defects, the severe the curve downward concave.

Stage-II: the curve section linearly developed tells that the compaction of defects has finished and the rock is undergoing elastic deformation. The higher the angle of the section line inclined, the stronger the rock.

Stage-III: the upward-concave curve section tells that there are new fractures developing inside the rock. The plastic deformation starts, and the new generated fractures together with the initial defects are possible to cause friction between its two side-faces.

Stage-IV: the curve section turning to drop tells that the fractures are getting wider, longer and to connect with each other. The rock is losing its strength and stability, and the final fracturing failure or rock hazard is impending.

For the difference between rock compositions, the details of stress-strain curve of different rock will be different. As to brittle rock, its stage-II is close to point P and its stage-IV will be cliff-shaped. Usually, most of the crust rocks are brittle. Five kinds of typical crust rock, granodiorite, gabbro, gneiss, limestone and marble had been tested in our experiments. The typical load-displacement curves of the tested rock samples are shown in Figure 14. It tells that all the tested rocks are brittle.

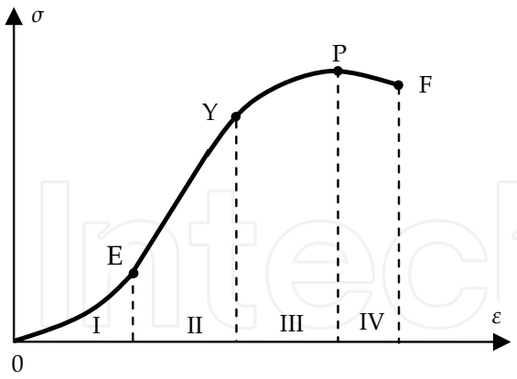

Fig. 13. Typical AIR*T* curve of uni-axially loaded rock

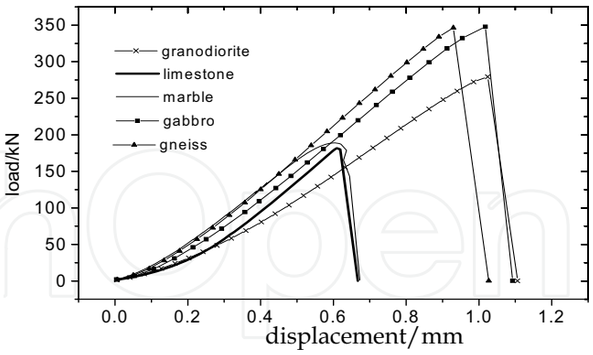

Fig. 14. The load-displacement curves of five tested rocks

2) The influence of loading condition

The experiments discovered that the evolutions of AIR*T* have different laws in different loading condition, such as uni-axial loading (constant displacement controlled), compressively-sheared loading (approximately constant load controlled) and bi-axial loading (constant displacement controlled).

a) Uni-axial loading

As shown in the left-hand side of Figure 15, the surface facing to the infrared imager is to be detected, and a rectangle region close to the boundary of the rock sample is defined for data resampling and analyzing (Liu et al., 2002; Wu et al., 2002). Multiple experiments revealed that there was slight variation of AIR*T* at different deformation stage although the AIR*T* linearly increased with load and deformation. At stage-I, the AIR*T* will rise slowly or drop a little; at stage-II, the AIR*T* will rise stably; at stage-III, the AIR*T* will rise quickly than that in stage-I and stage-II. The right-hand side of Figure 15 shows the comparison of the evolution of AIR*T* and the load with rock deformation, which is rock displacement in generally, of a marble sample.

b) Compressive-shear loading

In condition of compressively shear, the rock sample will always get fracturing along the shearing plane, which locates near to the central plane of the loaded sample. To minimize data resampling work and to focus on the key region, a narrow rectangle along the shearing plane is defined as the resampling and analyzing region (Wu et al., 2004c). Multiple experiments revealed that the temporal evolution of the AIR*T* is different with the shearing angle. Three shearing angles (γ) being 45^o, 60^o and 70^o respectively, are applied. As the shearing angle changes from 45^o to 70^o, the temporal evolution changes from monotonic rise, to drop-to-rise and to monotonic drop in order, as in Figure 16.

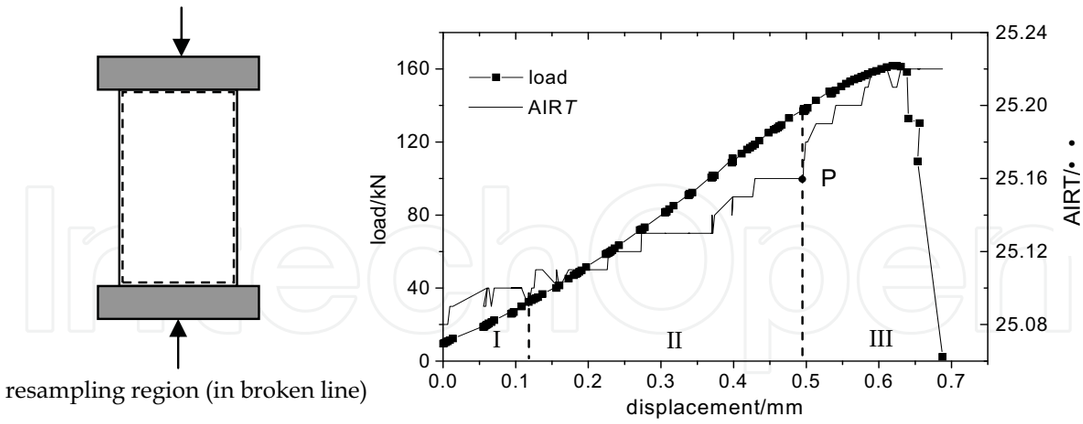

Fig. 15. The typical AIR*T* curve of uni-axially loaded rock sample (marble)

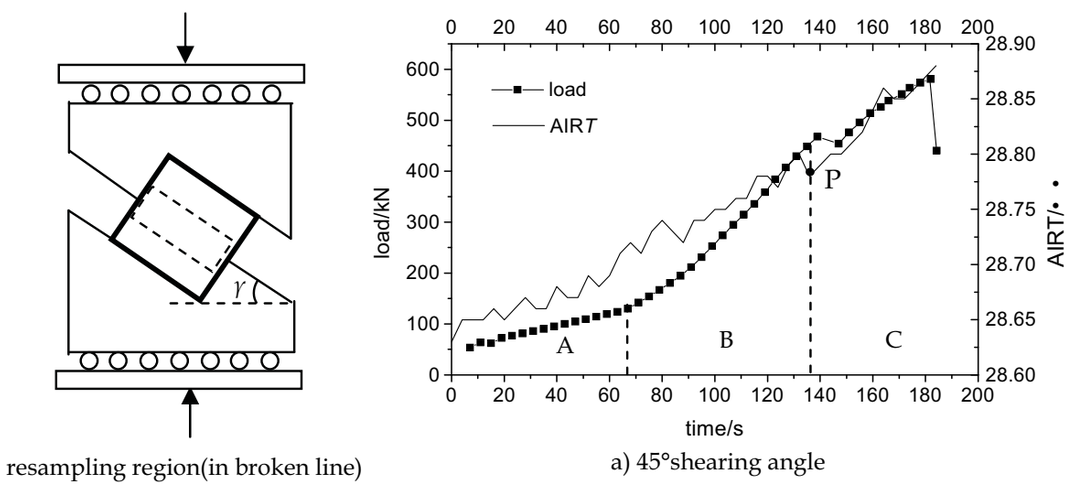

a) 45°shearing angle

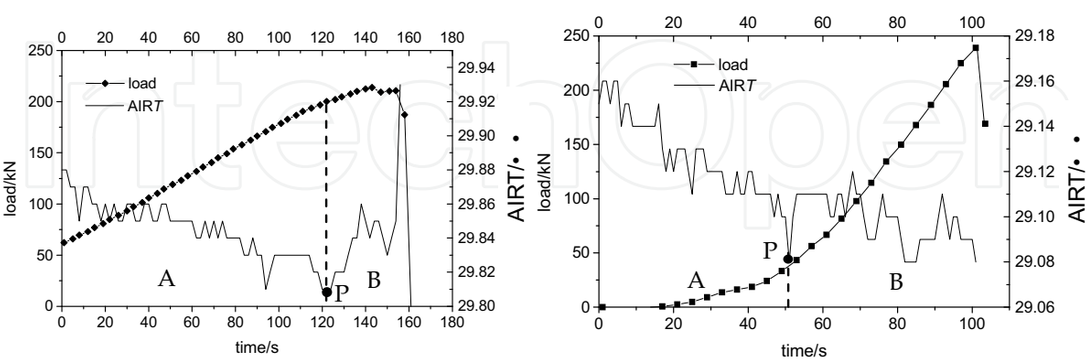

b) 60°shearing angle c) 70°shearing angle

Fig. 16. The typical AIR*T* curve of compressively-sheared rock samples at different shearing angles

The mechanism lays in that the ratio of compressive-stress to shear-stress along the shearing plane decrease with the rise of the shearing angle. The smaller is the shearing angle, the higher is the compression-shear ratio. In condition of 45^o, the load-time curve developed in three stages, as stage A, B and C in Figure 16a, with load increasing from slow to rapid, and to slow again. In condition of 60^o the load-time curve developed in two stages, as stage A and B in Figure 16b, with load speed changing from approximate constant to be decrease slightly. In condition of 70^o, the load-time curve developed in two stages, as stage A and B in Figure 16c, with loading speed changing from slow to rapid.

The compressive action on loaded rock is to cause surface IRR temperature rise, while the tensile action on loaded rock is to cause surface IRR temperature drop. Actually, both compressive action and tensile action are to occur along the compressively sheared plane, and the detected surface IRR is the comprehensive effect of the two actions. It was reached that (Wu et al., 2004c): 1) in condition of shearing angle being 45^o, the surface AIR*T* will rise monotonically with loading in that the temperature increment from compressive action and friction is stronger than the temperature decrement from tensile action in the whole loading process; 2) in condition of shearing angle being 60^o, the surface AIR*T* will drop monotonically with loading in that the temperature increment from compressive action and friction is weaker than the temperature decrement from tensile action before stage-III (point Y in Figure 13, and point P in Figure 16b); with the friction effect getting strong in stage-III, the surface AIR*T* will get to rise in that the temperature from compression and friction get stronger than the temperature decrement from tensile action; 3) in condition of 70^o, the surface AIR*T* will drop monotonically with loading in that the temperature increment from both compression and friction are weaker than the temperature decrement from tensile action.

c) Biaxial loading

By using of bi-axial loading system and infrared imaging system, the IRR features of two kinds of disjointed jointed faults, respectively be collinearly and non-collinearly disjointed faults, were experimentally studied (Wu et al., 2004a). Since all the faults got fractured finally at the disjointed zone, a circle covering the disjointed region is defined as the resampling region, as in the left-hand side of Figure 17. It could be known from the right-hand side of Figure 17 that the IRR from loaded samples is related with load stress, and the evolution stage could be classified into five stages (I~V) relating with initial compacting, elastic deforming, stress blocking, stress deblocking and rock fracturing respectively. From stage-II to stage-IV, the evolution of AIR*T* has the features of rising to dropping, and to rising again.

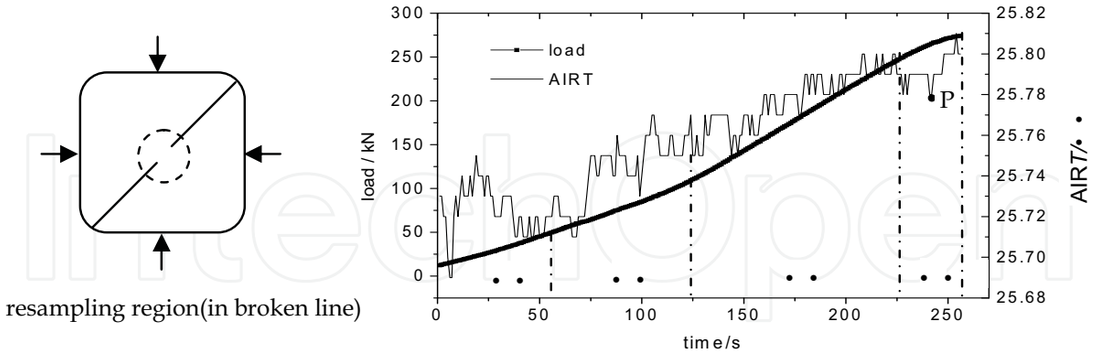

a) collinearly disjointed faults

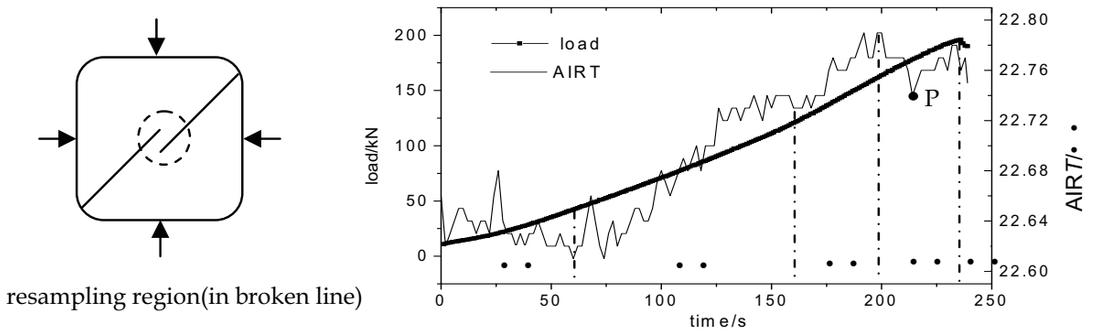

b) en echelon disjointed

Fig. 17. The typical AIR*T* evolution of two kinds of disjointed faults bi-axially loaded

3) The influence of rock characteristics

It was discovered in our experiments that for the most of rock samples in condition of uni-axial loading, its AIR*T* approximately rose with loading. But there were a few abnormal samples made from limestone had shown AIR*T* features of dropping with loading, as in Figure 18. The cause lies in that limestone has much more pores than the other rocks. Usually, there are many gases, such as CH_4, CO_2, CO and O_2 etc., enclosed inside the pores of rock body (Wang, 2003). With the decrement of pore volume due to the loading compaction and with the increment of fractures produced inside the limestone sample, the pore gases will get escaping. The escaping behavior of pore gas needs to absorb thermal energy from the rock sample. If the heat from compression and friction is lower than that absorbed by pore gases, the surface AIR*T* is to drop with loading. If look carefully at the load-displacement curves in Figure 14, it could be founded that the curve of limestone concaved downward the most at the compaction stage as compared to that of the other four kinds of rock, which means that there are more pores inside limestone than the others.

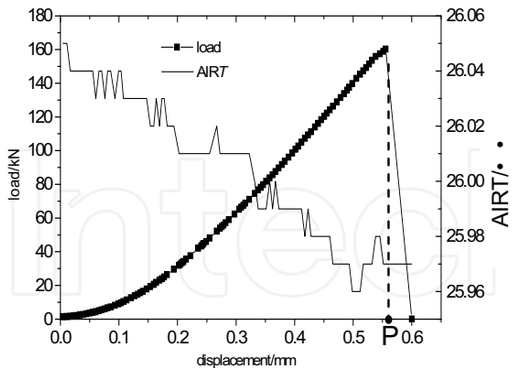

Fig. 18. AIR*T* of uni-axially loaded limestone sample

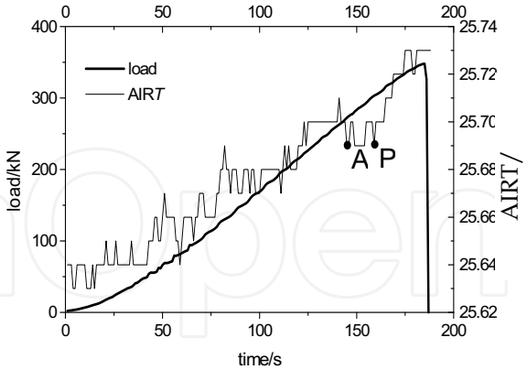

Fig. 19. AIR*T* short-dropping precursor for uni-axially loaded gabbro sample

2.3.3 The classification of precursors

Analysis to the evolution of AIR*T* curves discovered that a large amount of rock samples in condition of uni-axial loading, compressively-sheared loading and bi-axial loading had presented obvious precursors for rock fracturing. As referring to the general process of AIR*T* evolution, the AIR*T* anomaly precursors for rock fracturing and hazard could be classified as short-dropping, rapid-rising and dropping-to-rising respectively.

1) Short-dropping precursor

The AIR*T* curve rises with loading but has a short dropping at loading stage-IV; later, the AIR*T* curve will rise again. The bi-axially load on collinearly and non-collinearly disjointed faults had shown short-dropping precursors as in Figure 17, and the point P was suggested to be the precursor point of rock fracturing and rock hazard. Figure 19 shows another typical case of gabbro sample uni-axially loaded. Here, point A is the turning point of AIR*T* from rising to short dropping, and point P is another turning point from short dropping to rising again, which is suggested to be the precursor point of rock fracturing and rock hazard.

2) Rapid-rising precursor

The AIR*T* curve rises slowly with loading but turns to rise rapidly before rock fracturing, and the turning point is exactly the precursor point. Figure 15 and Figure 16a have this kind of precursor. Figure 20 shows another typical case of marble sample uni-axially loaded. Here, point P is the turning point of AIR*T* from rising slowly to rising fast, which is suggested to be the precursor point of rock fracturing and rock hazard.

3) Dropping-to-rising precursor

The AIR*T* curve drops slowly with loading but turns to rise just before rock fracturing, and the turning point is exactly the precursor point. Figure 16b has this kind of precursor. Figure 21 shows another typical case of marble sample uni-axially loaded. Here, point P is the turning point of AIR*T* from dropping slowly to rising fast, which is suggested to be the precursor point of rock fracturing and rock hazard.

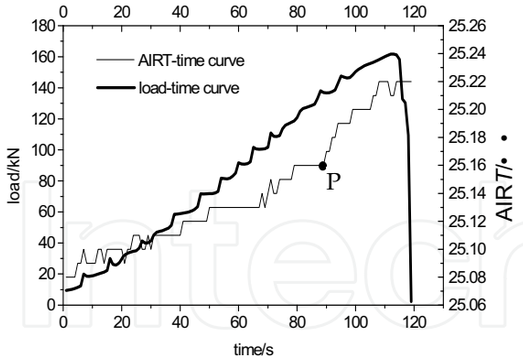

Fig. 20. AIR*T* fast rising precursor for uni-axially loaded marble sample

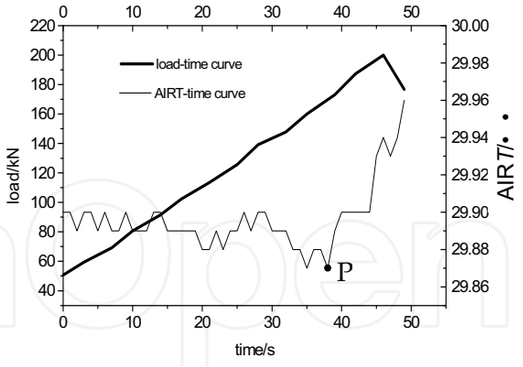

Fig. 21. AIR*T* dropping-to-rising precursor for compressively sheared loaded marble sample

2.3.4 The temporal features of precursors

The occurrence moments of the precursors of AIR*T* of totally 52 tested rock samples are listed in Table 1(Wu et al, 2006b). Although the loading conditions and the rock samples are different, the precursor occurrence moment, were very similar as 0.77~0.94σ_c(σ_p). Here, σ_c is the uni-axial compressive strength, and σ_p is the peak stress. The precursor occurrence moment of uni-axially loaded or compressive sheared rock sample is 0.79σ_c and 0.82σ_c respectively. It is worthy to mention that the precursor occurrence moment of bi-axially loaded collinearly disjointed faults and echelon faults are much different. That for collinearly disjointed faults was close to the peak stress, 0.87σ_p, while that for echelon faults was far away from peak stress, 0.77σ_p. It provides an important evidence for the complexity of study on tectonic EQ prediction on shock time, based on satellite infrared remote sensing and referring to the seismogenic mechanism.

Loading condition	Sum of tested samples, *St*	Sum of samples with precursors, *Sp*	The ratio: (*Sp*/*St*)• • 100%	Average of precursor occurrence moment
uni-axial loading	22	9	41%	0.79σ_c
compressively-sheared loading 70• •	7	1	14%	0.94σ_p
compressively-sheared loading 60• •	8	6	74%	0.82σ_p
compressively-sheared loading 45• •	11	8	73%	0.77σ_p
compressively-sheared loading (58%)				
Bi-axial loading for collinearly disjointed faults	2	2	100%	0.87σ_p
Bi-axial loading for en echelon faults	2	2	100%	0.77σ_p

Table 1. Statistic for precursor occurrence in different loading conditions

2.4 Large IRR at Fracturing Centre

As the recording rate of the infrared imager applied was 60f/s, the transient IRR

temperature at the fracturing center could be snapped. In condition of uni-axial loading, the fracturing center of a brittle rock is usually at the "X"-shaped fracturing center. It is discovered that the transient IRR temperature at the fracturing center is much higher than that on rock surface, as in Figure 22, and it is positively related with rock strength and rock deformation. For some compressively sheared hard rock samples made from gabbro and gneiss, the transient IRR temperature at the fracturing center is higher than 155°C, which is the upper limitation of the 2nd temperature range (72~155°C) of the imager applied.

In condition of high angle, 60• and 70°, compressively sheared loading, the fracturing center is at the center of the fractured shearing zone. Since the ruptured upper block of rock sample was pushed apart from the steel platen immediately after the abrupt rupturing, usually be 1~2 s after the rupturing, the inside shearing zone got exposed to the imager immediately and the transient IRR temperature filed was snapped. It was discovered that the IRR temperature on the inside shearing zone is not only much higher than that of outside rock surface, but also inhomogeneous distributed, neither even nor centripetal, as in Figure 23. It means that much more mechanical energy had been converted into frictional thermal and IRR energy due to the intensive energy accumulation, the sufficient local deformation and the abrupt frictional sliding at the center of the shearing zone. In other words, the large IRR temperature at the inside shearing center had reflected the comprehensive effect of local concentrated energy conversion and frictional thermal.

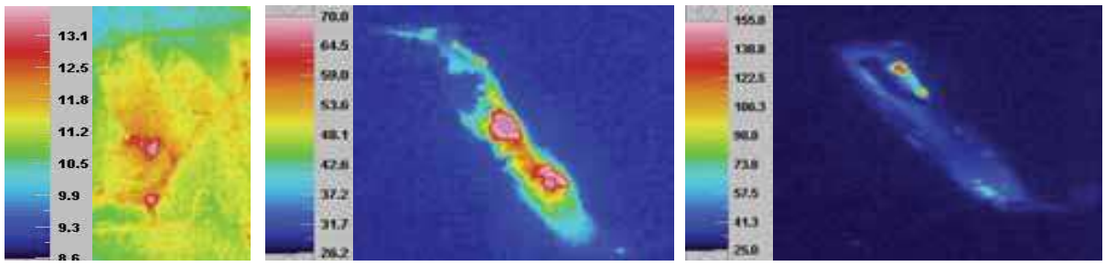

a) uni-axially loaded granite b) compressively sheared gabbro-1 c) compressively sheared gabbro-2

Fig. 22 The transient IRR thermograme of fracturing rock samples

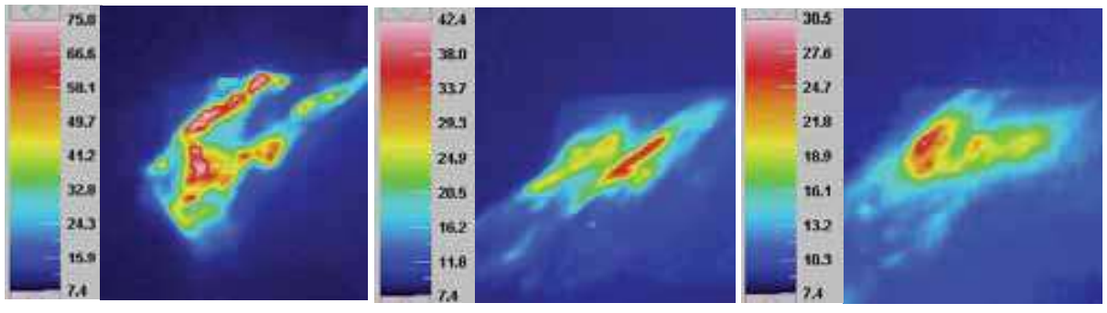

(a) marble-1 (b) marble-2 (c) granite

Fig. 23. The inside IRR isothermal filed on the fracturing zone of compressively sheared rock samples

Hence, it could be deduced that in condition of great tectonic stress, large deformation

and/or abrupt frictional sliding, large temperature as high as hundreds or thousands of degree Celsius is possible inside crust rocks. The high temperature could cause partial melt of crust rock, which provides a scientific explanation for the existence of pseudotachylyte in some lager faults (Nicolas et al., 1977; Sibson et al, 1980) and for the failure-generated EQ lights (Martelli et al., 1989). Besides, we can deduce that the continuous shearing deformation or the abrupt fracturing of highly loaded rock/coal body in a coal mine is possible to cause local sheared heating of temperature hundreds of degree Celsius, which might be a potential ignition of local methane (the minimum ignition temperature is 595°C).

3. Remote Sensing Rock Mechanics Model (RSRM-model)

3.1 Thermo-Mechanical Coupling Effect

3.1.1 Thermo-mechanical coupling in a loaded solid

The heat production inside a loaded solid is called as thermo-mechanical coupling effect. According to the material features and the different deformation stages of a loaded solid, the thermo-mechanical coupling is classified as thermo-elastic, thermo-plastic and thermo-viscous respectively for elastic deformation, plastic deformation and viscous deformation. Generally the rock is a hard brittle solid, its plastic and viscous deformation could be ignored, and the thermo-elastic effect and the frictional thermal are the two chief mechanisms of surface IRR from loaded rock. Kelvin coined the thermo-elastic theory in 1853 that the changed physical temperature of a loaded component is correlated to its changed stress as follows:

$$\Delta T / T = -K_0 \Delta\sigma \tag{1}$$

Here: T is the absolute temperature of a loaded component (K); ΔT is the changed temperature (K); K_0 is the thermo-elastic factor (MPa^{-1}); and $\Delta\sigma$ is the changed sum of three principal stresses ($\sum\sigma_i, i = 1,2,3$, MPa).

As for an isotropic linear elastic solid loaded bi-axially with a free surface, the surface physical temperature variation is tightly correlated with the sum of two principal stresses ($\sum\sigma_i, i = 1,2$):

$$\Delta T = -\alpha / \rho C_p \cdot [T \cdot \Delta(\sigma_1 + \sigma_2)] \tag{2}$$

Here: T is the surface absolute temperature of a loaded solid (K); ΔT is the changed temperature (K); α is the factor of linear expansion (K^{-1}); ρ is the solid density (Kg $\cdot$ m^{-3}); Cp is thermal capacity of solid at normal atmosphere (J $\cdot$ Kg^{-1} $\cdot$ K^{-1}); σ_1 and σ_2 are the two principal stresses (MPa). The thermo-elastic factor K is defined as $K = -\alpha / \rho C_p$.

For the mechanism of stress measurement with TSA and SPATE, the relationship between the stress increment and the IRR signal based on equation (2) is as follows (Mounatin and Webber, 1978):

$$\begin{aligned} \Delta(\sigma_1 + \sigma_2) &= A_{th} \cdot \Delta S \\ \Delta S &= \Delta(\sigma_1 + \sigma_2) \cdot A_{th}^{-1} \cdot \end{aligned} \tag{3}$$

Here: A_{th} is a comprehensive factor called as corrective factor, which is a function of solid surface emissivity, solid surface physical temperature, solid thermo-elastic factor and three parameters related to the IRR detector, unit in MPa· U-1. ΔS is the increment of thermo-elastic voltage signal detected (U).

3.1.2 Changed IRR temperature of loaded rock

If the slight change of rock surface emissivity, rock thermo-elastic factor and the physical parameters of IRR detector during rock loading could be ignored, and if the changed rock surface physical temperature cannot be ignored due to the thermal exchange and the frictional thermal, the relationship between A_{th} and changed rock surface physical temperature could be expressed as $A_{th} = \beta \cdot T^{-1}$. The detected IRR signal S is a direct representation of surface IRR temperature, i.e., $\Delta \mathrm{IRR}T = \gamma \cdot \Delta S$. Hence, the following equation for changed IRR temperature could be deduced:

$$\Delta \mathrm{IRR}T = \gamma \cdot \beta^{-1} \cdot T \cdot \Delta(\sigma_1 + \sigma_2) \tag{4}$$

Here: $\Delta \mathrm{IRR}T$ is the changed IRR temperature (K); β is a constant correction factor related to rock surface's emisivity, rock thermo-elastic factor and three parameters of IRR detector, in unit MPa·K·U-1; γ is a transfer factor between detected voltage signal and IRR temperature (K·U-1).

It means in equation (4) that the changed IRR temperature of rock surface is a direct reflection of the changed sum of the two principal stresses. If no frictional thermal produced and the thermal exchange is stable, the IRR temperature of rock surface is to rise with loading, and the spatial-temporal evolution of surface IRR image will be stable. If there is no frictional thermal produced but the thermal exchange is unstable, the surface IRR temperature will be unstable, and the spatial-temporal evolution of surface IRR image will also be unstable. If there is frictional thermal produced inside and conducted to rock surface, both the thermal exchange and the surface IRR temperature of rock surface will be unstable, and the spatial-temporal evolution of surface IRR image will get complicated, as in Figures 2~5, 10, 11.

Especially, in condition of compressive shearing and fictional sliding, there is a large amount of frictional thermal produced in the friction zone, which is to cause the rise of physical temperature in friction zone. The rock surface temperature will rise if the thermal conduction from the friction zone can reach to rock surface. Hence, the IRR image anomaly will be distinguished and sometimes be large as a combined effect of rock stress and frictional thermal, as in Figures 6~9.

3.2 Remote Sensing Rock Mechanics model

3.2.1 Energy-Related IRR from Loaded Rock

As a relatively independent closed system comprised of loader head, rock sample and environmental air, as in Figure 24, the rock deformation, rock fracturing and rock hazard are all of a complex process of energy input and consumption. If the possible chemical reactions inside a loaded rock can be ignored, the inputted energy of a loaded rock will include the mechanical work from loader and the heat input through positive thermal exchange from loader head and environmental air. The energy consumption by the loaded rock is much more complex including the energy accumulation in rock and the energy dissipation from rock.

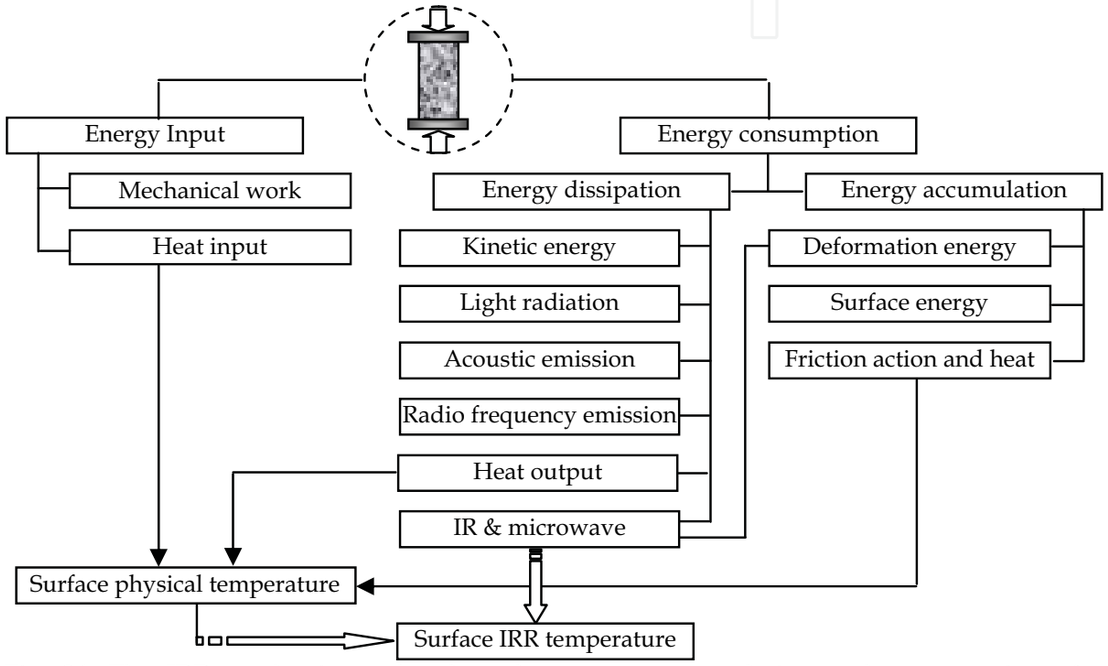

Fig. 24. The IRR mechanism related to the energy accumulation and consumption of a loaded rock

The energy accumulation in a loaded rock includes the positive elastic-plastic deformation energy of rock (the positive change of oscillation and rotation energy of mineral molecules), the surface energy of new produced fractures or fissures, and the friction actions between mineral molecules, grains, joints, fissures and fractures inside the rock as well as thus produced frictional thermal. The energy dissipation from loaded rock includes the negative thermal exchange with the loader head and/or environmental air (i.e., heat output), the kinetic energy of departed fragments of fractured rock, the light radiation, acoustic emission, radio frequency emission and IR & microwave radiation.

The thermal exchange and the friction action are to change the heat state of a loaded rock, and the rock surface physical temperature is a direct index reflecting the heat state of the loaded rock. Stephen-Boltzmann law states that the IRR strength (radiation flux density) of any material, at temperature above absolute zero degree, is biquadratic to its surface physical temperature. Crystal Physics states that the energy jump of molecules oscillation and/or rotation due to the change of molecules distance, resulting from deformation, is an

important mechanism of electromagnetic radiation. Hence, rock surface IRR is a comprehensive effect of rock deformation and rock surface thermal state. Rock surface IRR temperature could be a detective index reflecting rock surface physical temperature and rock surface deformation field, which implicating the complex physical-mechanical process inside the loaded rock.

In spite of thermal exchange and plastic deformation, the thermo-elastic effect and the frictional thermal are two of the main mechanics of changed IRR from loaded brittle rock. In the stage of elastic deformation, the thermo-elastic effect is the main cause; while in the stage of plastic deformation or fracturing, the friction-thermal effect plays a great role. At the moment of rock fracturing or hazard, the fraction-heat effect gets more distinguished. The frictional thermal effect depends on two factors being frictional force (decided by normal stress and frictional coefficient) and frictional speed respectively. The larger the frictional force and the quicker the frictional speed, the more the frictional heat.

3.2.2 RSRM-model based on independent system

The rock sample, load header and environment air could be taken as a closed independent system, as in Figure 25, and the energy of the loaded rock sample is in a balance state as follows:

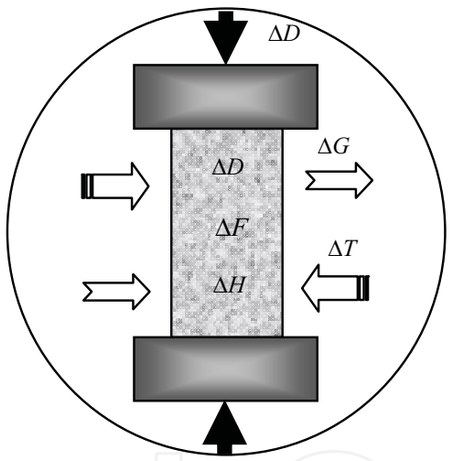

Fig. 25. The energy balance of a loaded rock sample in a closed independent system

$$\Delta M + \Delta T = \Delta D + \Delta F + \Delta H + \Delta G \tag{5}$$

Here: ΔM • • The inputted mechanical energy from loader, J; be positive;

ΔT • • The inputted thermal energy from loader and environment air, J; be positive;

ΔD • • The produced deformation energy of rock sample in elastic and plastic state, J; be positive;

ΔF • • The sum of consumed rock fracturing energy and formed fracture surface energy, J; be positive;

ΔH • • The heat energy increment of rock decided by its physical temperature, J; be positive if temperature rise or be negative if temperature drop;

ΔG • • The energy consumed by the desorbing and escaping of pore gas in rock samples, J; be positive.

From equation (5) we have:

$$\Delta H = (\Delta M + \Delta T) - (\Delta D + \Delta F + \Delta G) \tag{6}$$

The change of heat energy will result in the change of physical temperature• surface radiation energy and IRR temperature of loaded rock samples. Referring to Stephen-Boltzmann law, the $\mathrm{AIR}T$ is a direct index of rock radiation energy, and the change of $\mathrm{AIR}T$ ($\Delta A\mathrm{IR}T$) must have certain a relationship with the physical temperature (T) of loaded rock sample as:

$$E_{IR} = f(\mathrm{AIR}T) = \varepsilon\sigma T^4 \tag{7}$$

Here: E_{IR}• • The radiation energy of a loaded rock, J;

$\mathrm{AIR}T$ • • The surface average IRR temperature of a loaded rock, K;

ε • • The radiation factor of rock sample, $0 < \varepsilon < 1$;

σ • • The constant of Stephen-Boltzmann, $\sigma = 5.6679 \times 10^{-8}$, J• m• 2• K• 4• •

Thermo-elastic effect is the basic mechanism of changed IRR from a loaded rock sample. Moreover, the desorbing and the escaping of pore gas, the expanding of initial fissures or joints, the friction between fissures, fractures, joints and grains, the thermal transfer between the rock, loader header and environment air, and the radiation from the environment all are to have thermal effect on loaded rock samples. The thermal state is comprehensively affected by the six factors which are rock stress, pore gas desorbing & escaping, rock fracturing, heat transferring, rock frictionating and environment radiation respectively. The equation could be expressed as follows:

$$\begin{aligned} \Delta A\mathrm{IR}T &= f[\Delta(\sigma_1 + \sigma_2), \Delta G, \Delta F_1, \Delta H, \Delta F_2, \Delta E] \\ &= f_1(t) + f_2(t) + f_3(t) + f_4(t) + f_5(t) + f_6(t) \end{aligned} \tag{8}$$

Here: $\Delta A\mathrm{IR}T$ • • The detected change of $\mathrm{AIR}T$, K; be positive if rise, be negative if drop;

$f_1(t)$ • • IRR temperature change due to thermo-elastic effect ($\Delta(\sigma_1 + \sigma_2)$, K; be positive or negative;

$f_2(t)$ • • IRR temperature change due to pore gas adsorbing & escaping (ΔG), K; be negative• •

$f_3(t)$ • • IRR temperature change due to the production of new fractures and the expansion of initial fissures, joints and new produced fractures (ΔF_1), K; be negative;

$f_4(t)$ • • IRR temperature change due to frictional thermal (ΔF_2), K; be positive;

$f_5(t)$ • • IRR temperature change due to heat transfer (ΔH), K; be positive or negative.

$f_6(t)$ • • IRR temperature change due to environment radiation (ΔE), K; be positive.

1) Thermo-elastic effect: $f_1(t)$

Referring to thermo-elastic theory and equation (4), $f_1(t)$ could be calculated as:

$$f_1(t) = \gamma \cdot \beta^{-1} \cdot T \cdot \Delta(\sigma_1 + \sigma_2) \tag{9}$$

In condition of uni-axially compressive loading, the load is to cause temperature rise in that σ_2 is constant zero and the positive σ_1 will linearly increase with loading. If $\Delta\sigma_1$ is positive, the $f_1(t)$ will be positive; If $\Delta\sigma_1$ is negative, the $f_1(t)$ will be negative. Hence, the $f_1(t)$ will be positive before the compressive stress peak, and will turn to be negative after the compressive stress peak.

In condition of uni-axially tensile loading, the load is to cause temperature drop in that σ_2 is constant zero and the negative σ_1 will linearly increase with loading. If $\Delta\sigma_1$ is positive, the $f_1(t)$ will be positive; If $\Delta\sigma_1$ is negative, the $f_1(t)$ will be negative. Hence, the $f_1(t)$ will be negative before the tensile stress peak, and will turn to be positive after the tensile stress peak.

In condition of compressively-sheared loading, the rock sample will be compressed by the normal component of the load. However, as to the central shearing plane, it will suffer not only compressive stress but also shearing stress. The σ_1 refers to the positive compressive stress normal to the shearing plane, while the σ_2 refers to the shearing stress which is actually negative tensile stress along the shearing plane. Hence, the $\Delta A\mathrm{IR}T$ is decided by the sum of compressive stress and the tensile stress. If $\Delta(\sigma_1 + \sigma_2) > 0$, the $f_1(t)$ will be positive; If $\Delta(\sigma_1 + \sigma_2) < 0$, the $f_1(t)$ will be negative. As to Figure 1c, it's easy to know that $\Delta(\sigma_1 + \sigma_2)$ will be positive if the shearing angle $\gamma < 45^0$, $\Delta(\sigma_1 + \sigma_2)$ will be zero if the shearing angle $\gamma = 45^0$, $\Delta(\sigma_1 + \sigma_2)$ will be negative if the shearing angle $\gamma > 45^0$.

2) Pore gas desorbing & escaping effect: $f_2(t)$

Any rock has pores of different size more or less inside. Some rock, especially the sedimentary rock, may has certain gas, such as CH_4, CO_2, CO and O_2, enclosed in the pores or/and absorbed on the pore surface (Wang, 2003; Yang et al., 1999). Usually, most of the pores are enclosed and the gas molecules stay inside both in free gassy state and absorbed state. If the rock is loaded and suffers deformation, the volume of pores will decrease which results in the escape of gas from the pores. Once the load and deformation cause the enclosed pores getting fractured, the gassy molecules will escape firstly and the absorbed molecules will get desorbed to be gassy molecules and escape later. Both desorbing and escaping actions need to make use of heat energy from the rock, and thus will result in the

AIR*T* drop of rock surface. Hence, the $f_2(t)$ is always negative, and the more the pores and gas enclosed, the more the negative effect of $f_2(t)$.

3) Fracture effect: $f_3(t)$

With loading and deforming, the rock is to get fractured. The new produced fractures together with the initial fissures and joints will extend both in width and length. The production of new fractures needs to consume energy, and the extension of fissures, joints and fractures also needs to consume energy. Hence, the $f_3(t)$ is always negative, and the more the fractures produced and fissures, joints and fractures extended, the more the negative effect of $f_3(t)$.

4) Frictional thermal effect: $f_4(t)$

With loading and deforming, the friction action is to occur between rock fissures, rock joints, rock grains, and new produced fractures. The friction action could be interpreted as: 1) at the beginning stage of loading, the friction may only be resulted from between rock fissures and between rock joints; 2) later, rock deformation increases with loading, new fractures are produced, and the friction between rock grains and between new produced fractures will join in; 3) finally, at the ending stage of loading, the rock deformation and fractures will be sufficiently developed, and the frictions between rock grains and between new produced fractures will be the chief contributors to the frictional thermal. In a word, the $f_4(t)$ is always positive no matter what is the principle friction factor. The more the friction, the more the positive effect of $f_4(t)$.

5) Heat transfer effect: $f_5(t)$

In the process of loading and inside the respectively independent loading system, the heat exchange is inevitable between the rock sample and the load header, the shearing platen or cushion-blocks, the surrounded atmosphere, etc. If the current temperature of rock sample is higher than the others, the heat of rock sample will be transferred out to whose temperature is lower. If the current temperature of rock sample is lower than the others, the heat of the others will be transferred into rock sample. Hence, the temperature of rock sample is a dynamic balance behavior between the heat transferred in and the heat transferred out. If the heat transferred in is more than that transferred out, the $f_5(t)$ will be positive; otherwise, it will be negative.

6) Environment-radiation effect: $f_6(t)$

The IRR detected by infrared imager includes not only the direct radiation from rock surface itself, but also the reflected radiation from environment. In laboratory, the chief environment radiations are the scattering sunshine, the moving human bodies and the illumination lamp. For the uncertain change of scattering sunshine, the movement of human bodies before the loaded rock sample, and the fluctuation of illumination light, the environment radiation effect on rock sample will be random. Hence, sometimes $f_6(t)$ may be positive, but sometimes $f_6(t)$ be negative. To eliminating the environment-radiation effect, the human bodies inside the laboratory were not permitted to move during testing process, the illumination lights were turned off, and the windows as well as its curtains were closed. Furthermore, some experiments were conducted in the evening so as to avoid the scattering sunshine completely.

3.3 Experiment Interpretation with RSRM-Model

Due to the comprehensive effects of $f_1(t) \sim f_6(t)$, the evolution of AIR*T* will be complex and will result in different possibility for abnormal AIR*T* precursors in different rock loading conditions, which including the loading scheme, rock type, and environment parameters. The following discussions are based on that $f_5(t)$ and $f_6(t)$ can be ignored.

3.3.1 Uni-axial loading experiments

For uni-axially loaded rock, $f_4(t)$ will take place only after that the rock has sufficiently deformed and the fractures have sufficiently developed.

At loading stage I and stage II, the rock surface AIR*T* are decided by $f_1(t)$ and $f_2(t)$. If the loaded rock is igneous rock or metamorphic rock, $f_2(t)$ is very rare since no gas absorbed in its pores usually, and the AIR*T* will rise with loading. If the loaded rock is sediment rock and with gas closed and absorbed in pores, $f_2(t)$ is inevitable, and the AIR*T* will rise if $f_1(t) > |f_2(t)|$, or be constant if $f_1(t) = |f_2(t)|$, or drop if $f_1(t) < |f_2(t)|$.

At loading stage III, fractures get sufficiently developed and pores get seriously damaged. The $f_3(t)$ begins to has more and more effect on evolution process of AIR*T*. AIR*T* will rise if $f_1(t) > |f_2(t) + f_3(t)|$, or be constant if $f_1(t) = |f_2(t) + f_3(t)|$, or drop if $f_1(t) < |f_2(t) + f_3(t)|$.

At loading stage IV, the friction action starts and $f_4(t)$ begins to have more and more effect on the evolution of AIR*T*. AIR*T* will rise if $[f_1(t) + f_4(t)] > |f_2(t) + f_3(t)|$, or be constant if $[f_1(t) + f_4(t)] = |f_2(t) + f_3(t)|$, or drop if $[f_1(t) + f_4(t)] < |f_2(t) + f_3(t)|$. Since $f_2(t)$ is very rare for igneous rock or metamorphic rock, the rise speed of AIR*T* of loaded igneous rock or metamorphic rock will get fast at stage IV, and the speed turning point is suggested to be the precursors point.

3.3.2 Compressive shearing experiments

For compressively sheared rock, not only $f_1(t)$ but also $f_4(t)$ is decided by shearing angle (γ). If $\gamma < 45^0$, $f_1(t)$ will be positive for $\Delta(\sigma_1 + \sigma_2) > 0$, and the friction action will be much strong in that σ_1, which is normal to the friction plane, is large. If $\gamma = 45^0$, $f_1(t)$ will be zero since $\Delta(\sigma_1 + \sigma_2) = 0$. If $\gamma > 45^0$, $f_1(t)$ will be negative for $\Delta(\sigma_1 + \sigma_2) < 0$, and the friction action will be much week since σ_1 is slight.

3.3.3 Biaxial loading experiments

For bi-axially loaded rock, $f_1(t)$ will always be positive. As to bi-axially loaded en echelon faults, collinearly and non-collinearly disjointed faults, $f_2(t)$, $f_3(t)$ and $f_4(t)$ will occur

simultaneously, and the evolution of AIR*T* will be fluctuated. If $[f_1(t)+f_4(t)]>|f_2(t)-f_3(t)|$, AIR*T* will rise; if $[f_1(t)+f_4(t)]=|f_2(t)-f_3(t)|$, AIR*T* will keep in the same level, and if $[f_1(t)+f_4(t)]<|f_2(t)-f_3(t)|$, AIR*T* will drop. Usually, the fact is that $[f_1(t)+f_4(t)]<|f_2(t)-f_3(t)|$ at the fracturing stage, and there is a short drop of AIR*T*, which is called as 'silence' before EQ (Ohtake et al., 1981). However, $f_4(t)$ will be an important factor at the later stage of loading for the concentrated formation of fractures and friction in the disjointed zone, and the final state of AIR*T* will be rise for $[f_1(t)+f_4(t)]>|f_2(t)-f_3(t)|$.

4. Earthquake Thermal Infrared Anomalies

The prediction of EQ is very difficult, but it's not impossible. A number of signs warning of EQs, such as foreshock activities, peculiar animal behaviour, increased low frequency EM-noise, concentrations of radon in water and air, ionosphere and magnetosphere perturbation, radio frequency emissions, terrestrial gas emanations, EQ clouds, and satellite TIR anomalies, have been proposed and reported during the past centuries. Satellite TIR anomaly was firstly reported in 1989, and had been repeatedly verified in the world during the past 20 years. It is becoming a prospecting space observation technology for seismic activity monitoring and for EQ predicating.

4.1 General Features of EQ TIR Anomaly

Gorny (1988) firstly reported that there were large area of TIR anomalies in METEO satellite remote sensing images, spatial resolution being 5 Km and wave length being 10.5~12.5μm, before many moderate-strong tectonic EQs in the mid-Asia and the east-Mediterranean region. Tronin (1996) analyzed 10000 about TIR images of channel AVHRR-2 of NOAA in ten years for the mid-Asia, and reached that there existed average anomaly, 1~5℃, before the EQs at this region, and that there was obvious statistical relations between the EQ and TIR anomaly. Qiang (1990), Cui (1999), Liu (1999), Xu (2000), Zhang(2002), Ouzounov(2004), Arun (2005), Liu (2007), Wu (2008) also reported that there occurred TIR anomalies in satellite images (NOAA, FY, MODIS) days before more than 100 EQs in Asia (China, India, Iran, Japan, Kamchatka, Pakistan, Turkey) and Europe (Italy, Greece, Spain). Analysis to all the reported cases, it was uncovered that satellite TIR anomaly before EQ has the following features generally (Wu et al., 2009):

1) Temporal features: Satellite TIR anomaly usually appears 1~26 days before shock, and reaches to its peak 1~2 days before shock, and will disappeared soon after shock.
2) Spatial features: The spatial distribution and geometrical shape of TIR anomaly is tightly related with tectonic structures such as plate borders and active faults. With the EQ impending, the TIR anomaly will move to or extend to gradually the coming epicentre along the structures.
3) Temperature features: the temperature of the TIR anomaly is usually 2~6℃ higher than that of outside or surrounding the TIR anomaly.
4) Magnitude features: there are positive relations somewhat between the TIR

anomaly energy (the anomaly area times the anomaly temperature) and the magnitude of future shock.

4.2 Anomalies Interpretation with RSRM-Model

The RSRM experimental results are applied to analyze satellite remote sensed TIR anomalies before several strong EQs in Asia. Referring to the seismogenic mechanisms, the satellite TIR anomalies are in good accordance with the detected IRR anomalies from rock fracturing and seismogenic experiments with fault system being simulated with disjointed faults and intersected faults.

4.2.1 Dongsha Ms5.9 EQ 1992 in Taiwan, China

Dongsha Ms5.9 EQ occurred in Taiwan on Sept 14, 1992. The NOAA satellite images show that there was TIR anomaly appeared along the regional faults and downfaulted basins before shock as in Figure 26 (Wu et al., 2006c). There was an isolated and spoon-shaped high temperature area to the southwest of Taiwan Island 25 days before shock (Aug 19, 1992). The head of 'spoon' locates in the downfaulted basin-• •and the handle of 'spoon' distributes along fault-6. Satellite TIR image on Aug 22 shows that the high temperature on 'spoon head' diminished, but the TIR anomaly on 'spoon handle' became wide. Later, the anomaly moves gradually to the epicenter. TIR image on Sept 9 shows that a large area of high temperature had appeared around the coming epicenter, and the maximum temperature (in brown color) appeared south-close to the coming epicenter. It indicated that the TIR anomaly was consistent with the regional tectonic structures (faults and basins) in spatial position and geometry.

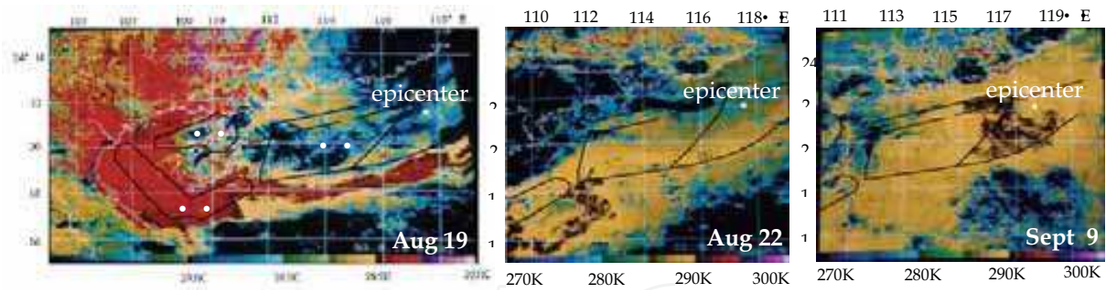

Fig. 26. Satellite TIR anomaly images before Dongsha Ms5.9 EQ (Sept 14, 1992)

4.2.2 Zhangbei Ms6.2 EQ 1998 in China

Zhangbei Ms6.2 EQ occurred in China at 11:50 am, Jan 10, 1998. With the overlay of the active fault system investigated and deduced, in red lines, on night time NOAA satellite infrared images, as in Figure 27, it was discovered that (Wu et al., 2007b): 1) 18 days before shock, Dec 28, 1997, the TIR images on land and sea surface are basically normal, and the contours of TIR temperature field of Bohai Bay appeared to be along the coastline; 2) 5 days before shock, Jan 5, 1998, there occurred a positive TIR anomaly strip from Bohai Bay to Zhangbei passing through Beijing, its temperature was 3°C higher than that of outside, and the contours of TIR temperature field of Bohai Bay got offset the coastline; 3) 1 day before shock, Jan 8, 1998, the positive TIR anomaly strip had got wider and its temperature was 7°C higher than that of outside, and the contours of TIR temperature field of Bohai Bay got in accordance with the positive TIR strip; 4) 1 day after shock, Jan 11, 1998, the pattern of TIR

images on the surface of land and sea turned to be normal again.

There are several disjointed active faults along the positive TIR strip, including a possible uncovered great active deep fault going from Bohai Bay to Zhangbei. Besides, to the southwest of Zhangbei, there are two small active faults pointing to Zhangbei. If extend the three faults respectively towards Zhangbei, it could be found that Zhangbei is exactly the intersection point. Hence, the tectonic background around the epicenter is basically comprised of three intersected active faults as two groups, i.e., the primary fault is the independent one from Bohai Bay to Zhangbei, and the secondary two act as another group. The two groups of faults split basically the regional crust into three geo-blocks (geo-block A, B and C_1+C_2) as the RSRM experiment model in Figure 28b (rock block A, B and C), and the secondary two faults act as the two sides of an acute wedge-shaped geo-block (geo-block C_2) as the RSRM experiment model in Figure 28d (rock block C). The geometric features of the faults and the spatio-temporal features of TIR anomaly were similar. Therefore, the mechanical mechanism of Zhangbei EQ should be classified to be the failure of an intersected active fault system, which with an acute wedge-shaped geo-block being its secondary active object.

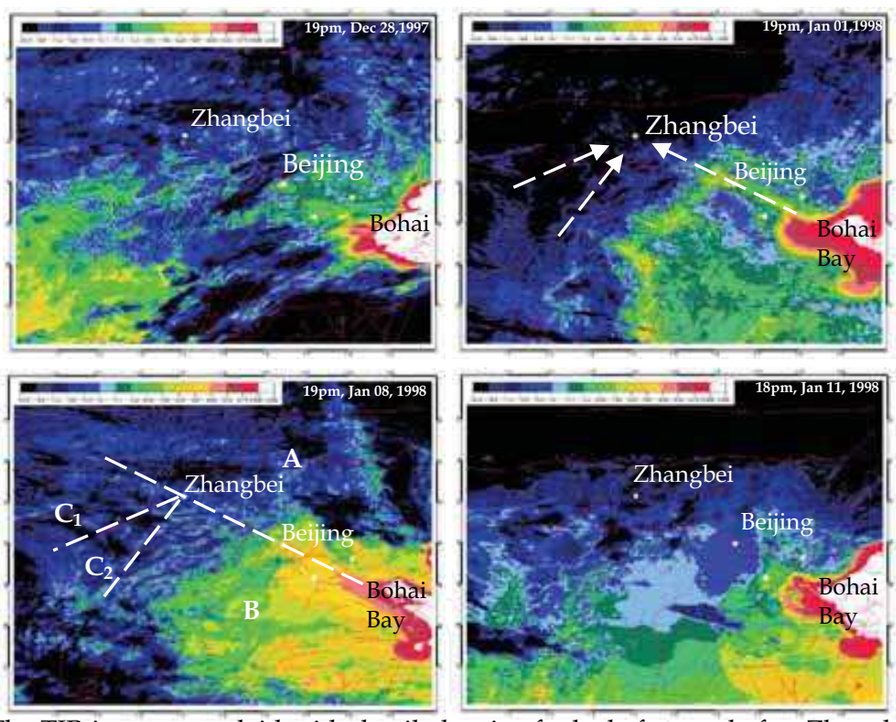

Fig. 27. The TIR images overlaid with detailed active faults before and after Zhangbei Ms6.2 EQ (Jan 10, 1998)

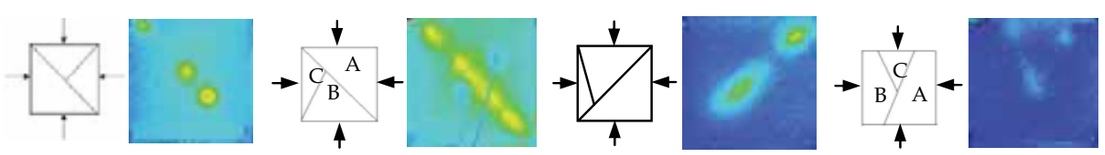

a) 90° intersection b) 75° intersection c) 60° intersection d) 40° intersection

Fig. 28. The IRR anomaly features of simulated tectonic activities due to bi-axially load (Wu et al., 2007b)

4.2.3 Izmit Ms 7.8 EQ 1999 in Turkey

Izmit Ms 7.8 EQ occurred in Turkey on Aug 17, 1999. In the epicenter zone, there were two en echelon tectonic faults, and the epicenter is 45km about to the west of the disjointed place of the two en echelon faults, as in Figure 29. With thermal image of Aug 1&2 being the reference, the differential thermal images from Aug 6 to Aug 26 were obtained, and it was revealed that there were NOAA satellite TIR anomaly at the disjointed zone of two en echelon faults since Aug 6 , 11 days before shock (Tronin, 2000), as in Figure 29. The RSRM experiments on the simulation of tectonic EQ due to the fracturing of disjointed faults had revealed that there were IRR anomaly increment and concentrated deformation at the disjointed zone, as in Figure 30. Obviously, the spatial features of NOAA TIR anomaly before Izmit Ms 7.8 EQ were the same as that of IRR anomaly before the fracturing of disjointed faults.

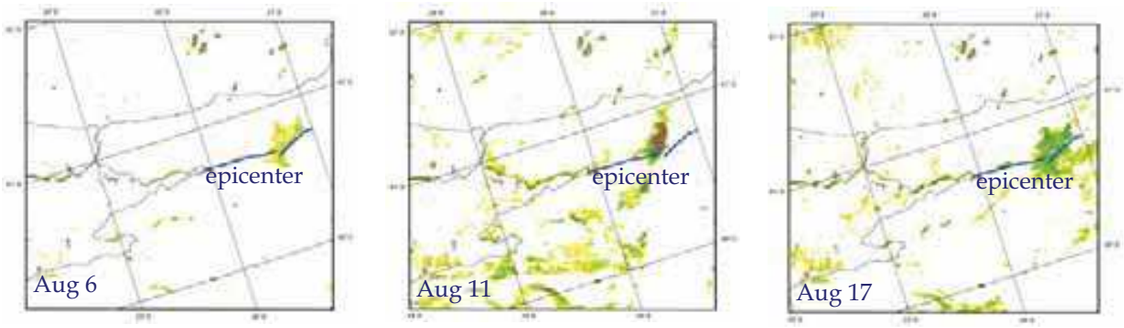

Fig. 29. TIR anomalies 0~11 days before Izmit Ms 7.8 EQ (Aug 17, 1999)

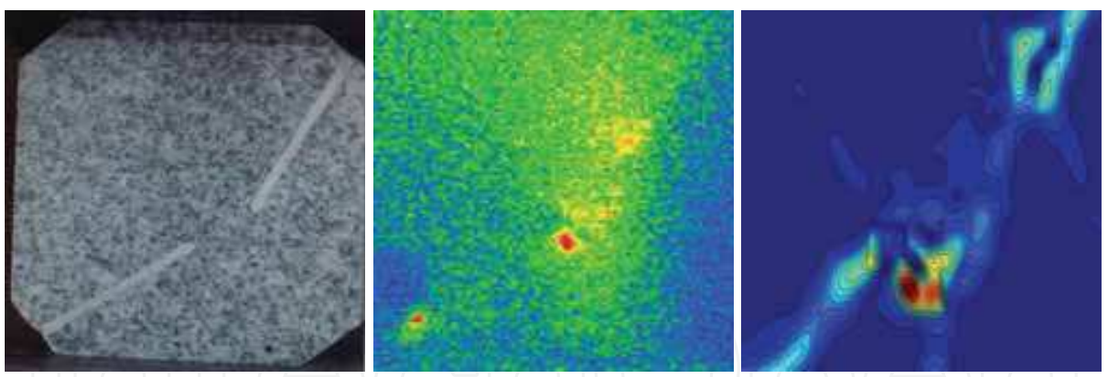

Fig. 30. The IRR anomaly and deformation concentration of a bi-axially loaded granite sample with disjointed faults

4.2.4 Hengchun Ms7.2 EQ 2006 in Taiwan, China

Hengchun Ms7.2 EQ occurred in Taiwan at 12:26pm, Dec 26, 2006. TIR images from stationary satellite FY-2 showed that there was TIR anomaly nearby the coming epicenter. The TIR anomaly appeared to the east of Philippines six days before shock, and moved gradually toward west to Philippines. Later, the anomaly changed its direction to the north, and the temperature increased 10^{o}C about one day before shock. Figure 31 shows that the satellite TIR images around Hengchun on Dec 25, 2006 (Liu et al., 2007). A disjointed thermal strip (in orange color) appeared on the southwest of Taiwan at 1:00am, and

developed gradually to be an X-shaped thermal anomaly zone at 10:00am. The epicenter located closely to the cross point of the X-shaped zones. The evolution process of satellite TIR images was very similar to that of X-shaped thermal IRR anomaly in RSRM experiments as in Figure 2.

4.2.5 Wenchuan Ms8.0 EQ 2008 in China

Wenchuan Ms8.0 EQ occurred in China at 14:28 am, May 12, 2008. The epicenter locates at the transferring zone of Tibetan Plateau to Sichuan Basin, which is only 92Km to the NW of Chengdu, the capital of Sichuan province. Analysis to FY-2C TIR images, as in Figure 32, it is discovered that there was an high temperature strip with length of 3 000 km appeared on April 23, 20 days before shock, which started from India Plate and developed to northeast along the east front of Tibetan and Loess Plateau (Wu et al., 2008). The cause might be the great accumulation of fictional sliding stress along the east foreland of Tibetan and Loess Plateau due to the subduction of India Plate to Euro-Asia Plate. The east foreland of Tibetan and Loess Plateau act as the fictional sliding plane between the west part of China (including Tibetan and Loess Plateau) and the east part of China (including the North, Middle and Southwest China). The evolution of satellite TIR images was similar to that of detected strip-shaped IRR anomaly in the fictional sliding experiments as in Figure 8 and Figure 9, which shows the evolution of TIR anomaly along the sliding plane.

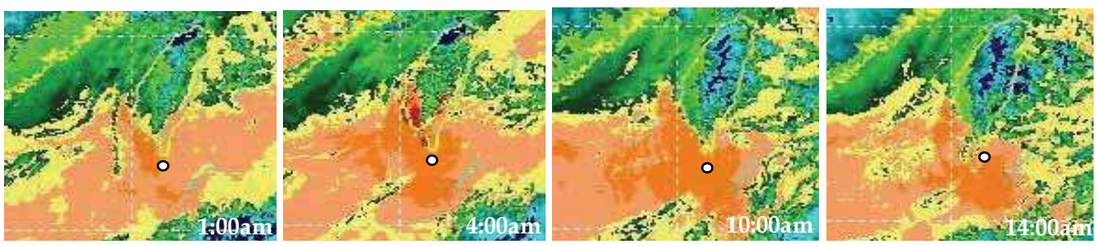

Fig.31. Satellite TIR images one day before Hengchun Ms7.2 EQ (Dec 25, 2006)

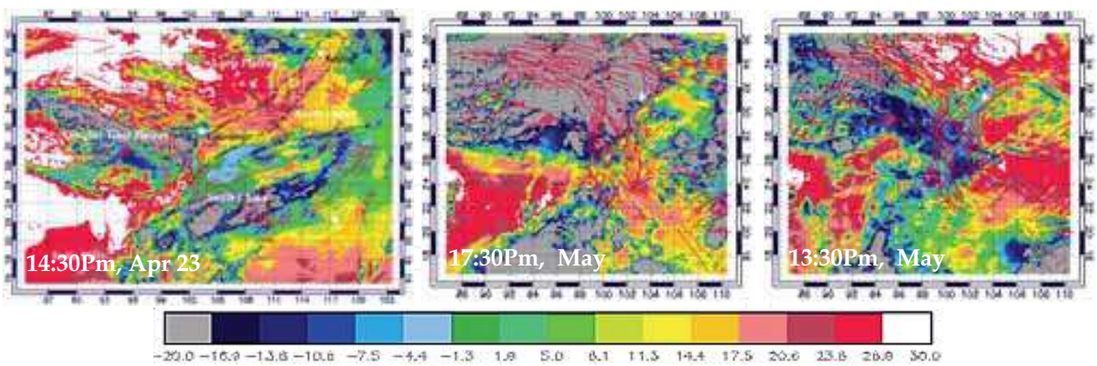

Fig.32. Satellite TIR images before Wenchuan Ms8.0 EQ (May 12, 2008)

5. Future Researches

5.1 On RSRM Experiment

As a detectable remote sensing signal related with rock stress and physical temperature, IRR is a meaningful index for studying rock load, rock deformation, rock fracturing and rock

hazard. The temporal evolution of surface IRR from loaded rock is the comprehensive effect of rock thermo-elastic acting, pore gas desorbing & escaping, fractures producing & extending, rock frictionating, heat transferring and environment radiation. The IRR image anomaly referring to the spatial-temporal evolution of IRR from loaded rock is an important precursor for rock fracturing, and will be meaningful for the predication of geo-hazards including tectonic EQ. For the practical application of RSRM, deeper research on IRR imaging detection quantitatively and specially on rock stress and rock hazard for experimental rock mechanics, rock engineering, tectonic activity and strong EQ is demanded.

The mechanism of experimental detected IRR anomaly can be theoretically interpreted by taking the load header, the rock sample and the environment to be a closed independent system in energy balance state. There are two of the main rock-physics mechanisms, respectively being thermo-mechanical coupling and frictional thermal due to tectonic stress, rock fracturing and fictional sliding, for the change IRR from loaded rock samples (Wu, et al., 2006c). Besides, positive hole (P-hole) activation due to piezoelectricity was suggested to be another mechanism of IRR from loaded quartz-bearing igneous rock (Freund, 2002), such as granite, basalt, diorite, and gabbro.

To search for scientific interpretation on the relations among satellite TIR anomaly, rock stress and experimentally detected IRR anomaly, the EM transferring process from underground rock body to satellite sensors, through lithosphere, earth surface coversphere (including soil layers, water bodies and vegetations), the atmosphere and lithosphere, should be systematically studied. Pulinets pointed out that the incubation of an EQ is to disturb the ionosphere (Pulinets, 1998), and it was suggested that lithosphere-atmosphere-ionosphere (LAI) coupling is the mechanism of satellite TIR anomaly before strong EQ (Molchanov et al., 2004). Nevertheless, the action of earth surface coversphere on the transferring and the magnifying of EM signals from underground loaded rock to atmosphere should not be ignored, even if its physical mechanism are not clear. For the scientific interpretation of satellite TIR anomaly before strong EQ, the lithosphere-coversphere-ionosphere (LCA) coupling is the key, while for the scientific interpretation of ionosphere anomaly, the lithosphere-coversphere-atmosphere-ionosphere (LCAI) coupling should be focused. However, present experiments on LAI, LCA and LCAI coupling are rather insufficient. Future experiments specially designed to uncover the mechanisms & laws and to construct the models & quantitative equations of LAI, LCA and LCAI couplings are expected.

5.2 On EQ Thermal Infrared Anomaly

Although there are uncertain influences from meteorological variation, satellite TIR anomaly has quite different identification features from that of unseismology-resulted TIR anomaly. Satellite TIR remote sensing is becoming a prospecting technique for monitoring tectonic activities and for predicting strong tectonic EQ, which provide a negativism to that EQ cannot be predicted. Anyway, the practical predication of EQ is not so easy. The regional tectonic background and the active fault system have extremely important affects on the incubation of EQ and the TIR anomaly. Especially, the intersected faults, compressively-sheared faults, and disjointed faults are to control the location and the routing of the spatial evolution of satellite TIR anomaly, and the brightest spot of TIR anomaly along the fault, or at the intersection point, or at disjointed zone of faults might

foretell the possible epicenter (Wu et al., 2007b).

First of all, massive observation information including crust stress, land deformation, atmosphere components, underground water, surface and near-surface temperature, satellite remote sensing TIR anomaly and EM disturbance in ionosphere should be integrated together for data fusion and cross checking to analyze comprehensively the tectonic activity and rock fracturing process. A grid-based distributed database and analysis tools on TIR remote sensing images, with global and regional tectonic structures being its background, should be set up to assist the extraction of EQ TIR anomaly in different temporal and spatial scale. Besides, a quantitative model for tectonic activity analysis and for EQ magnitude predication based on TIR anomaly should be developed.

The GEOSS under construction is to provide an integral and integrated monitoring on earth environment, Geo-hazard and global disasters. A generalized remote sensing (GRS) based on the integration of space-based, aero-based, near-surface based, in-situ based and underground-based monitoring is forming in the world (Wu and Liu, 2007). The international broad and sincere cooperation, inside the framework of GEOSS without discipline exclusion and data privacy, between seismologists, remote sensing scientists, meteorologists, geophysical scientists, geochemist and spatial information scientists in good faith is expected. Besides, a powerful spatial information system, especially for EQ early warning and short-coming prediction based on GEOSS, should be developed. It should has powerful functions such as massive information classification, smart theme mapping, easy map-layer overlay, fast features extraction, effective data fusion, intelligent data mine, powerful knowledge discovery, and easy access and share.

A possible technical procedure based on GRS for satellite TIR anomaly monitoring, analyzing and early warning of tectonic EQ inside the framework of GEOSS might be that: 1) the seismological geology background being the foundation of satellite TIR anomaly analysis; 2) the long-term GPS continuous monitoring and D-InSAR measurement being the guidance of tectonic stress detection and active fault identification; 3) the underground water temperature, near surface air temperature, radon & green gas, structural cloud anomaly dairy monitoring being the forerunner for preliminary identification of coming EQ; 4) the anomaly analysis of satellite TIR, NCEP temperature and ionosphere disturbance being the dominant for early warning of temporal-spatial-magnitude parameters of EQ; and 5) the additional celestial stress on active faults being a special leading disturbance for possible tectonic EQ.

6. References

Arun K. & Swapnamita C.(2005). Thermal remote sensing technique in the study of pre-earthquake thermal anomalies. *J. Ind. Geophys. Union*, 9(3):197-207

Brady B. & Rowell G. (1986). Laboratory investigation for the electrodynamics of rock fracture. *Nature*, 321(29): 488-492

Cui C., Zhang J. & Xiao Q.(1999). Monitoring the thermal IR anomaly of Zhangbei earthquake precursor by satellite remote sensing technique, *Proc. 20th Asia Remote Sensing Congress*, pp.1179-1184, Hongkong

Deng M., Qian J., Yin J., et al.(2001). Research on the application of infrared remote sensing in the stability monitoring and unstability prediction of large concrete engineering. *Chinese J Rock Mech. Engi.*, 20(2):147-50.

Freund F.(2002). Charge generation and propagation in igneous rocks. *J. Geodynamics,* 33(4-5): 543-570.

Geng N., Cui C. & Deng MD, et al.(1992). Remote sensing detection on rock fracturing experiment and the beginning of Remote Sensing Rock Mechanics. *ACTA Seismologic SINICA*, 14(supp) : 645-52.

Gorny V., Salman A., Tronin, A., et al.(1998). The earth outgoing IR radiation as an indicator of seismic activity, *Proc. Acad. Sci. USSR*, 30(1): 67-69.

Hudson J. & Harrison J.(1997). *Engineering rock mechanics*, Elsevier Science Inc., New York, pp.85-112

Liu D., Peng K., Liu W., et al. (1999). Thermal omens before earthquake. *Acta Seismologica Sinica*, 12(6):710-715

Liu S., Wu L., Li J. et al.(2007). Features and mechanism of the satellite thermal infrared anomaly before Henchun earthquake in Taiwan Region. *Science & Technology Review*, 25(6): 32-37

Liu S., Wu L., Wu Y., et al.(2002). Quantitative study on the thermal infrared radiation of dark mineral rock in condition of uni-axial loading. *Chinese J. Rock Mech. & Engi.,* 21(11): 1585-89

Luong M.(1990). Infrared thermovision of damage processes in concrete and rock. *Engi. Fracture Mechanics*, 35 (1~3): 127-35.

Martelli G., Smith P. & Woodward A.(1989). Light, radiofrequency emission and ionization effects associated with rock fracture. *Geophy. J. Int.*, 98(2): 397-401.

Molchanov O., Fedorov E., Schekotov A. et al.(2004). Lithosphere-atmosphere-ionosphere coupling as governing mechanism for preseismic short-term events in atmosphere and ionosphere. *Natural Hazards and Earth System Sciences*, 4: 757–767

Mounatin D. & Webber J.(1978). Stress pattern analysis by thermal emission (SPATE), *Proc. Soc. Photo-Opt. Inst. Engi*, 164:189.

Nicolas A., Bouchez J., Blaise J., et al.(1977). Geological aspects of deformation in continental shear zones. *Tectonophysics*, 42(1):55-73

Ohtake M., Matumoto T. & Latham G.(1981). Evaluation of the forecast of the 1978 Oaxaca Southern Mexico earthquake based on a precursory seismic quiescence. In: *Earthquake Prediction Maurice Ewing Series American Geophysics Union 4*）, pp.53-62

Ouzounov D. & Freund F.(2004). Mid-infrared emission prior to strong earthquakes analyzed by remote sensing data. *Adv. Space Res*. 33: 268-273.

Pulinets S. (1998). Seismic activity as a source of the ionospheric variability. *Adv. Space Res.*, 22(6): 903–907

Qiang Z., Xu X. & Dian C.(1990). Thermal infrared anomaly-precursor of impeding earthquakes. *Chinese Science Bulletin,* 35(17): 1324-1327

Renata D.(1977). Electromagnetic phenomena associated with earthquakes. *Geophsical survey*, 3(2):157-174.

Sibson R. et al.(1980). Power dissipation and stress levels on faults in the upper crust. *J. Geophysical research*, 85(B11): 6239-6247.

Thomson W.(1853). *Trans. R. Soc. Edinburgh*, 20: 83-261.

Tronin A.(1996). Satellite thermal survey—a new tool for the studies of seismoactive regions. *J Remote Sensing*, 17(8): 1439-1455

Tronin A.(2000). http://www.iki.rssi.ru/earth/ppt/tronin.ppt

Wang X.(2003). A research on the inorganic carbon dioxide from rock by thermal simulation experiments. *Advance in Earth Science*, 18(8):515-20

Wu L. & Liu S.(2007a). Generalized remote sensing for solid Earth hazards under condition of GEOSS. *Science & Technology Review*, 25(6): 5-11

Wu L. & Wang J.(1998). Infrared radiation features of coal and rocks under loading. *Int. J. Rock Mech. & Min. Sci* , 35(7):969-976

Wu L., Cui C., Geng N. et al.(2000). Remote Sensing Rock Mechanics (RSRM) and associated experimental studies. *Int J Rock Mech Min Sci*, 37(6): 879–88.

Wu L., Li J. & Liu S.(2009). Infrared anomaly analysis based on reference fields for earthquake remote sensing. *Seismology Geology*, 2009(in press)

Wu L., Li J., Xu X., et al.(2007b). Theoretical analysis to impending tectonic earthquake warning based on satellite infrared anomaly, *Proc. 2007 IEEE Int. Geosciences &Remote Sensing Symposium*, pp. 3723-3727

Wu L., Liu S, Shi W. et al.(2003). Experimental study on infrared anomaly of tectonic earthquake, *Proc. SPIE, Remote Sensing For Environmental Monitoring, GIS Applications & Geology Ⅲ*, 5239: 376-387.

Wu L., Liu S. & Wu Y.(2006c). The experiment evidences for tectonic earthquake forecasting based on anomaly analysis on satellite infrared image, *Proc. 2006 IEEE Int. Geosciences &Remote Sensing Symposium,* pp. 2158-216

Wu L., Liu S., Chen Y. et al.(2008). Satellite thermal infrared and cloud abnormities before Wenchuan earthquake. *Science & Technology Review, 26*(10):28-29

Wu L., Liu S., Wu Y. et al.(2002). Changes in IR with rock deformation. *Int. J. Rock Mech. & Min. Sci.*, 39(6): 825-31

Wu L., Liu S., Wu Y., et al.(2004a). Remote Sensing Rock Mechanics (Ⅰ) : laws of thermal infrared radiation from disjointed jointed faults fracturing and its meanings for tectonic earthquake omens. *Chinese J Rock Mech. & Engi.*, 23(1): 24-30

Wu L., Liu S., Wu Y., et al.(2004b). Remote Sensing Rock Mechanics (Ⅱ) : laws of thermal infrared radiation from bi-sheared faults friction sliding and its meanings for tectonic earthquake omens. *Chinese J Rock Mech. Engi.* , 23(2): 192-198

Wu L., Liu S., Wu Y., et al.(2004c). Remote Sensing Rock Mechanics (Ⅳ): laws of thermal infrared radiation from compressively-sheared fracturing rock and its meanings for earthquake omens. *Chinese J Rock Mech. & Engi.*, 23(4): 539-544

Wu L., Liu S., Wu Y., et al.(2006a). Precursors for rock fracturing and failure—part I: IRR image abnormalities. *Int J Rock Mech Mining Sci,* 43(3): 473-482

Wu L., Liu S., Wu Y., et al.(2006b). Precursors for rock fracturing and failure—part II: IRR T-curve abnormalities. *Int J Rock Mech Mining Sci*, 43(3): 483-493

Wu L., Liu S., Xu X., et al.(2004d). Remote Sensing Rock Mechanics (Ⅲ) : laws of thermal infrared radiation and acoustic emission from friction sliding intersected faults and its meanings for tectonic earthquake omens. *Chinese J Rock Mech. & Engi.*, 23(3): 401-407

Xu X., Xu X. & Wang Y. (2000). Satellite infrared anomaly before Nantou Ms=7.6 earthquake in Taiwan, China. *ACTA Seismologica SINICA*, 22(6): 656-659

Yamada I., Masuda K. & Murakami H.(1989). Electromagnetic and acoustic emission associated with rock fracture. *Phys. Earth Planet. Inter.,* 57(1-2):157-168.

Zhang Y. & Shen W.(2002). Satellite thermal infrared anomaly before the Xinjiang Qianhai boder Ms8.1 earthquake. *Northwestern Seismological J.*, 34(1): 1-4

IntechOpen

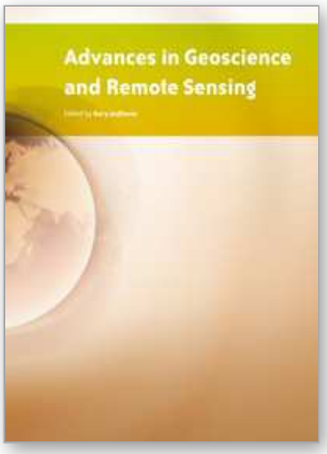

Advances in Geoscience and Remote Sensing

Edited by Gary Jedlovec

ISBN 978-953-307-005-6

Hard cover, 742 pages

Publisher InTech

Published online 01, October, 2009

Published in print edition October, 2009

Remote sensing is the acquisition of information of an object or phenomenon, by the use of either recording or real-time sensing device(s), that is not in physical or intimate contact with the object (such as by way of aircraft, spacecraft, satellite, buoy, or ship). In practice, remote sensing is the stand-off collection through the use of a variety of devices for gathering information on a given object or area. Human existence is dependent on our ability to understand, utilize, manage and maintain the environment we live in - Geoscience is the science that seeks to achieve these goals. This book is a collection of contributions from world-class scientists, engineers and educators engaged in the fields of geoscience and remote sensing.

InTech Europe
University Campus STeP Ri
Slavka Krautzeka 83/A
51000 Rijeka, Croatia
Phone: +385 (51) 770 447
Fax: +385 (51) 686 166
www.intechopen.com

InTech China
Unit 405, Office Block, Hotel Equatorial Shanghai
No.65, Yan An Road (West), Shanghai, 200040, China
中国上海市延安西路65号上海国际贵都大饭店办公楼405单元
Phone: +86-21-62489820
Fax: +86-21-62489821

IntechOpen